Issues in choosing the references to use for spectral ratios from observations and modeling, at Cavola landslide northern Italy

by

Paola Bordoni[1] , G. Di Giulio[1], A. J. Haines[2], F. Cara[1], G. Milana[1], and A. Rovelli[1]

1) Istituto Nazionale di Geofisica e Vulcanologia
Centro Nazionale Terremoti
Via di Vigna Murata 605
00143 Roma Italy.
2) Institute of Geological and Nuclear Sciences Limited (GNS Science)
764 Cumberland Street
Dunedin 9016, Otago, New Zealand

Submitting author:
paola.bordoni@ingv.it

Draft submitted to: Bullettin of the Seismological Society of America
9th December 2009

Abstract

A reference site has to be free of amplification or de-amplification effects, namely with no troughs and peaks in its Fourier amplitude spectrum. At the Cavola landslide we show that this spectrum is dependent on the direction of propagation of wave fronts for incidence angles in the range 30° to 90°. Our study is based on comparison of spectral ratios from observations and 2D numerical simulations. We have modeled propagation in a 2D profile for SH and SV waves with several incidence angles in the 0° ±90° range, where 0° and 90° are respectively vertical and horizontal incidence, except that ±90° denotes Rayleigh waves in the P-SV. We discuss in detail the result for angles of incidence of 0, ±20°, ±60°, ±90°. We have obtained observed horizontal-to-horizontal earthquakes spectral ratios using three reference sites. Two of these have matching receivers in the model, located at the opposite ends of the 2D profile. Overall observations are matched best when the reference site is located on the same side of the landslide as the incoming wave front. We also find general agreement of the observed H/H spectral ratios from earthquakes with H/V and H/H spectral ratios from noise, and the match between H/V values from noise and synthetic spectral ratios using an absolute, flat half-space reference is very good. On the other hand, 1D modeling performs poorly in comparison with 2D modeling in our case, for which the shape ratio h/D = 0.2 is intermediate between primarily-1D and strongly-2D wave propagation according to the classification of Bard and Bouchon (1985).

Introduction

Common empirical techniques widely used to quantify amplification at a site of interest are based on comparing recordings of earthquakes and cultural noise at a site of interest either to that of a reference site or to another component of motion. The reference response itself is then critical in such a computation. For earthquakes, the reference is usually a nearby site located on outcropping bedrock assumed to be representative of the excitation wave-field at the rock-sediment interface beneath the station of interest. However, previous studies have conclusively demonstrated that bedrock sites at the surface can be affected by amplification in the high-frequency band when compared to borehole bedrock sites, due to weathering of the surface bedrock (Steidl et al. 1996). Borehole seismometers would be an appropriate solution, but they should be located deep into the bedrock (Abercrombie, 1997). For seismic ambient noise, the reference is generally the vertical component recording at the site of interest, which is assumed to have negligible site amplification in comparison to the horizontal components. For numerical simulations, a synthetic from a corresponding flat half-space model is often used as the reference, and because of its nature is considered an 'absolute' reference. Such a reference cannot be achieved with actual observations, though borehole recording is likely to be the closest approximation.

There are very few study cases (e.g. Frischknecht and Wagner, 2004) where issues related to the direction of propagation of wave fronts have received attention in relation to the relative positions of a reference site and the site of interest. In this paper we will investigate these subjects. The idea of the 'absolute' reference will be tested as well, also in the context of the direction of propagation and angle of incidence of the waves. Our study is based on comparison of spectral ratios from observations and 2D numerical simulations for SH and P-SV seismic motion propagating into the model from its two opposite ends for a comprehensive set of incidence angles (0° to 90°).

A recent seismological experiment performed on the Cavola landslide, in a rural area of Northern Italy, has provided a very detailed observational dataset (Bordoni et al., 2007). The Cavola landslide was selected because its geologic and geophysical setting are common to many urban and rural areas of the Northern Apennines and its seismic response was of concern to the local authorities (Provincia di Modena, Provincia di Reggio Emilia and Regione Emilia Romagna) who co-funded the project and contributed to the site selection.

The landslide body is primarily made of clay and it slides over very old and highly fractured bedrock. These features result in a heterogeneous medium whose geometry is difficult to delineate definitively. To study its behavior in detail we installed over an area 130 m by 56 m 95 Guralp CMG-6TD 3-component seismometers provided by NERC-SEISUK. Three reference sites were chosen as the best available, in terms of rock firmness as well as accessibility, and the two we are most concerned with in this paper were instrumented with same equipment as the array.

We have selected a 2D profile across the array for a total length of 800 m, including 14 seismometers over a distance of 130 m, with a reference site at each end of the profile. The recordings within the array are strikingly different for coming from sites at such short separation, providing an excellent case-study for comparison to simulations. Along the cross section, landslide thicknesses as well as P and S wave velocity are well constrained from geophysical prospecting and also from the seismometer array recordings.

The paper is organized into spectral analysis of the observations, followed by spectral analysis of the synthetics. For the observations, having three reference sites available, one at each end of the 2D profile considered in the synthetics and a third at a similar distance from the array as the further away of these two, we have computed spectral ratios relative to all three. This is done for the same set of 10 local earthquakes, with averages and standard deviations computed for the individual stations in the array to identify which of the reference sites gives the most consistent spectral ratios. Then, to highlight azimuth related behavior of the propagation, we have selected 4 earthquakes coming from the two opposite back-azimuths in line with the 2D profile for the synthetics and present their individual spectral ratios relative to the two reference sites located at each end of the profile. To conclude the analysis of observations, we have computed H/V and H/H_{ref} spectral ratios from microseism in order to compare them to the earthquake H/H_{ref} spectral ratios.

In the modeling work, firstly we have computed synthetic spectral ratios relative to the reference site closest to the array in the 2D profile and compared them to the corresponding observed data computing the misfit. Secondly, we have repeated the first step using as reference the site located at the opposite end of the profile. Thirdly, to explain features in the results from the first two steps, we have looked at Fourier amplitude spectra of the synthetics at the reference sites. Fourthly, for comparison with H/V spectral ratios from noise we have

used a 1D flat half-space model as the reference. This has helped in developing ideas about absolute references, involving both horizontal and vertical components. Finally, we have compared spectral ratios from 2D and 1D modeling for incidence angles of 0°, 30° and 60°, to investigate to what extent 1D simulation could be a proxy for 2D simulation in our situation.

Geology, seismicity and geophysical site characterization

The Cavola landslide has a morphology, geology and urban setting typical of the Northern Apennines. Landslide hazard is high due to the geo-mechanical features of the rocks (Bertolini and Pellegrini, 2001). Nearly all the present landslides are ancient ones, dated back to Pleistocene and Holocene (Bertolini and Pizziolo, 2008), and are reactivated most commonly by sliding advancement along their body basal surface. Their morphology is characterized by a large crown, a narrow channel and large foot.

In particular, the Cavola landslide (Fig. 1) has a length of about 4 km and a thickness greater than 60 m at its foot, with an average slope of about 6° and about double that value in the foot area. It is made primarily of clay derived from marly-calcareous flysches deposited in a marine environment 70-83 million years ago (Monte Venere Formation and Monghidoro Formation, Plesi, 2002). In the Cavola area, firm outcrops consist of a highly fractured marl overlain by muddy and sandstone turbidite roughly half that age and belonging to the Monte Piano Marls Unit and Ranzano Sandstone Unit, respectively (Mancin et al., 2006).

In historical times there have been three instances of landslide activity triggered by meteorological events: the 1960 event was the most destructive involving an area of 1.3 km^2 and the total destruction of a settlement very close to the main Cavola village (Brunamonte, 1999). Even though historical activity has been triggered by meteorological events, rather than earthquakes, it is likely that the worst case scenario would be the coincidence of a meteorological event and an earthquake. Indeed, instrumental and historical seismicity indicate that high intensities of earthquake ground shaking are expected to occur at Cavola, and at all the other landslides in the Northern Apennines, on a timescale of several hundreds of years (Castello et al., 2006). Typical earthquake magnitude for the area is around 5; examples are the recent 23th December 2008, M_W=5.4 and 5.0, Northern Italy earthquakes (url: http://www.globalcmt.org). The biggest earthquakes in the historical catalogue were the

1920 Garfagnana and 1835 Alpi Apuane, about 40 km south-west of the Cavola landslide with intensities of IX to X MCS in their epicentral areas (Gruppo di lavoro CPTI, 2004).

The seismic array was deployed in a rural area adjacent to the Cavola village. To the west of the array Ranzano Sandstone Unit, hereafter RSU, outcrops (Fig. 2) while to the east the outcropping bedrock is the older and underlying Monte Piano Marls Unit, hereafter MPMU. Two boreholes, bh1 and bh3, existed prior to the experiment. At borehole bh1 the landslide is 45 meters thick and the bedrock belongs to the MPMU. Borehole bh3 is a very shallow, private borehole, with no information on the bedrock type but outcrops nearby belong to the RSU, which is then the more likely bedrock for bh3. Landslide thickness there is less than ten meters.

A variety of geophysical investigation were undertaken to characterize the experimental site (Bordoni et al., 2007), including geo-electrical, refraction and single-station noise measurements, as well as drilling of a new borehole, bh2, where down-hole P and S wave travel times were logged. At bh2 the landslide thickness is 25 m, with a 3 meters thick layer above the water table, and the bedrock is MPMU. As well, Vp and surface wave analyses (MASW) have been applied to seismic refraction profiles acquired adjacent to bh1 and bh2 on NNW-SSE lines, to infer P and S waves velocity as well as landslide thicknesses. Vp and MASW results agree with velocities and thicknesses obtained from bh1 and bh2.

Inferred values from down-hole logging of P velocity are 520 m/s in the top 3 m above the water table, 1630 m/s in the body of the landslide, and 2850 m/s in the basement. For S waves inferred interval velocities from borehole bh2 are 230 m/s above the water table and 625 m/s in the basement, while in the landslide body below the water table the S velocity appeared to increase approximately linearly with depth from about 300 m/s at the top to a value very close to that in the basement at the bottom. The average S wave velocity from refraction and MASW are 360 m/s within the landslide body, which is in agreement with average vertical travel times trough the landslide body obtained from the down-hole logging.

Data

From mid-July to mid-October 2004, an array of 95 Guralp CMG-6TD 3-component seismometers were deployed over an area 130 m by 56 m on the east flank of the Cavola landslide, with the northeastern-most station of the array, coded CAP3, on MPMU bedrock (Fig. 2). Each CMG-6TD instrument consists of a 24-bit digitizer and a three components sensor with a 30 s natural frequency. All the stations, except CACH, were powered by solar panels while absolute timing was provided by a GPS receiver connected to each seismograph. CACH, unlike the other instruments, was installed not on free-field but inside a church and suffered GPS and power failures. Therefore using this station, as we do in this paper, makes the earthquake dataset remarkably restricted compared to the whole earthquake dataset available. The sample rate initially set to 200 sps was swapped to 100 sps after the first 10 days of recording. During all the experiment the instruments were recording continuously.

Instruments were arranged in a grid-like configuration with inter-station spacing of 10 and 8 meters in the NE and NW directions respectively (Fig. 2), and with 27 meters of elevation difference. Including CAP3, three bedrock reference sites were instrumented. Station CAVA was on the same rock unit MPMU as CAP3, about 400 m to the north on the opposite side of the creek Rio di Pietra. Station CACH was on the RSU to the west of the array, which overlies MPMU at unknown depth.

For our 2D modeling, we have considered a NE-SW cross-section through the array (Fig. 2). It intersects boreholes bh1, bh2, bh3 and includes 14 of the array seismometers (coded from CAA3 to CAP3 following the Italian alphabet), and has a reference site at each end of the profile, namely site CACH at the southeast end of the profile and CAP3 at its northeast end. Table 1 lists the 10 local earthquakes (Fig. 3b) chosen for comparison with the modeling from among those recorded simultaneously at the three reference stations and at the array stations from a range of azimuths. Fig. 4a-b shows an example of recordings along the modeling line of one of these earthquakes. The low frequency band pass filtered (0.8-5 Hz) signals of Fig. 4a have the largest ground motion amplitudes at stations CAE3 to CAM3 in the middle part of the array where the topographic gradient is less strong, with clear differences between the N-S and E-W components. The same holds true for the E-W component of the high frequency band pass filtered signal (5-10 Hz), whilst the N-S component shows high amplification at stations located in the steepest part of the slope (Fig. 4b).

Data analysis

Noise spectral ratios

Noise at the Cavola array was affected throughout the day by strong variations in the amplitude and frequency content of the signal. Recent papers (Bordoni et al., 2009; and Cara et al., 2009) specifically investigate this feature, identifying as the dominant source of directional noise the working cycle of a nearby tiles factory (see Fig. 2). Because the intermittent noise is characterized by frequencies similar to those observed at the landslide (2.5-6 Hz), H/V analysis gives unstable values both in resonance frequencies and amplitudes making the identification of true resonance frequencies of the landslide through spectral ratios complex (see Cara et al. 2009 for details).

For our analyses we have selected a calmer period of noise not biased by this source, from 01:00 to 01:30 GMT on 8th of September 2004. We have computed the spectral ratios of the two separated horizontal components to the vertical component (Nakamura, 1989) at each site located approximately along line 3 of the Cavola array oriented in NE-SW direction. The spectral ratios of the horizontal components to reference spectra H_{ref}, for CAP3 and CACH sites have been calculated as well, given the limited size of the array and the closeness of reference and array sites. The reference H_{ref} was constructed as the root-mean-square Fourier spectral amplitude from both horizontal components in the following manner:

$$H_{ref} = \sqrt{\frac{NS^2 + EW^2}{2}} \quad (1)$$

The data have been split in 30 time intervals, each of 60s duration without overlap. The 60 sec windows were de-trended and tapered with a 5% Hanning window and fast Fourier transformed. The resulting Fourier amplitude spectra were smoothed using a 0.2 Hz running frequency window. The two horizontal components spectra for each time interval were then divided by the vertical component spectrum (H/V) or by the horizontal reference spectrum (H/H_{ref}). Finally the H/V and H/H_{ref} spectral ratios computed for each of the 60s windows were geometrically averaged over the window ensemble. All the analyses, both on noise and earthquakes,were performed using SAC2000 code (Goldstein et al. 2003).

Fig. 5 (a,b) shows the resulting noise H/V (Nakamura, 1989) and H/H_{ref} spectral ratios for the two horizontal components at a set of array sites for noise and earthquakes (the procedure for the earthquakes analyses are described later). In order to simplify the amount of data presented, here and in subsequent figures we present results for array sites CAB4, CAE3, CAG3, CAI3, CAM3, CAO3, CAP3 only. We have selected these sites as they have the same recorded dataset as the three reference sites (particularly CACH) and they sample the topography (and the array) at regular spacing.

Although the results in amplitude are not very different between H/V and H/Href , the H/V amplitude in principle cannot be used as an indicator of amplification effects occurring at a site during earthquakes. The difference in amplitude is likely due to the noise wave-field composition, in particular Bonnefoy-Claudet et al. (2008) pointed out the importance of Love waves contribution to the H/V amplitude.

The spectral ratios in Fig. 5 (a,b) show a systematic shift of the peak frequency from 2.8 Hz to 4 Hz moving downhill from site CAB4 to site CAM3. There is consistency between the three sets of spectral ratios both for the level of amplification and the frequency bands where it occurs, though H/H_{ref} using CACH reference site shows a higher amplification level However, due to the distance alone of CACH site from the array (about 600 m) H/H_{ref} results with CACH as reference could be biased by different noise source distributions at the reference station and the stations of interest. Otherwise, H/H_{ref} for noise and earthquakes are similar in amplification size and peak frequencies. At stations CAG3 and CAI3, located in the flat area, peaks do not have exactly the same frequencies but their differences are small (< 0.5 Hz). The latter shift has already been described by Cara et al. (2009) who interpreted it in terms of wave-field composition.

Properties of the reference sites

The H/H_{ref} results in Fig. 5 (a,b) highlight that there were issues with the reference sites that we have had to cope with. As already mentioned, these were the best sites available in terms of rock firmness as well as accessibility. CAP3 and CAVA were on the MPMU marl unit and CACH was on the stratigraphically higher RSU sandstone unit. Boreholes bh1 and bh2 adjacent to and within the array show that on that side of the landslide at least the landslide lies directly on the MPMU. The RSU bedrock at CACH, is underlain by the MPMU, and is of

unknown thickness and may not extend far, if at all, below the landslide. This would be of no consequence in our context if the RSU and MPMU had similar elastic properties, but that is likely not true.

The downhole logging at bh2 shows that immediately below the landslide at that point the S wave velocity of MPMU is 625 m/s, which is of order 0.4 times what would be expected in competent rock with the P wave velocity of 2850 m/s that was also measured there. This is indicative of the marl having been highly fractured, and possibly quite heterogeneous in its elastic properties. The effect of increasing pressure with depth means that cracks seal, so that at some point below the landslide there must be a transition from the fractured marl to proper bedrock. The only evidence possibly related to this in our geophysical investigations is a 1.2 Hz peak in H/V spectral ratio from noise (see Fig 5.), which is seen all over the landslide and at adjacent sites (Bordoni et al., 2007). Assuming an average S wave velocity of 1000 m/s for the fractured marl, this would suggest a depth to proper bedrock of order 200 m. The alternative is that the 1.2 Hz peak is a peculiarity of the noise source or sources.

Fig. 6 summarizes the spectral ratio data pertaining to the reference sites. The top panels show the H/V curves of noise. All three reference sites have standard bedrock characteristics, with flat spectra and values close to 1, though CAP3 appears to be slightly better in this regard than the other two sites. The remaining panels show H/H_{ref} values for earthquakes, with each of CACH, CAP3 and CAVA in turn providing the H_{ref} value, which is calculated as (1), in the same manner as outlined above for the noise data. Two sets of earthquakes are shown: the locations of group 1 (events 4-9-5-6 in Table 1) were in-plane with the line 3 through the array used in the 2D modeling, while group 2 (events 1-2-3-7-8-10) were out-of-plane (see Fig. 3b). Details of the processing are outlined below. The purpose of separating the two groups was to highlight possible directional effects. In fact no obvious differences are seen between the two sets of events.

What is clear, however, is that none of the earthquake H/H_{ref} spectral ratios for the reference sites is especially bedrock-like, as there are numerous peaks and troughs (Fig. 6). Overall the spectral ratios using CACH as reference show the largest amplitude, which means that CACH site has much lower response in earthquakes than CAP3 and CAVA. The reason could be that the S wave velocity of RSU sandstone is much more like that of genuine bedrock than the S wave velocity of the fractured MPMU marls. Even if this is correct, that doesn't mean CACH

is an ideal reference site, as the RSU is underlain by what may be a considerable thickness of MPMU.

In the remainder of the paper we will restrict ourselves to using CAP3 and CACH as reference sites, given that they are in the line 3 used in the numerical modeling (and were equipped with Guralp instruments, like the array sites on the landslide). Also, we have restricted the numerical modeling to considering only propagation in the fractured MPMU and the overlying landslide, by treating the MPMU as though it extended to infinite depth. Given that we know very little of the geometry and properties of the RSU, we have not included it in the modeling, and the price we pay for treating CACH as being on MPMU is that we cannot expect to model spectral ratios at all exactly with CACH as the reference site. Instead what we can look for is key trends, as we will explain.

Average spectral ratios from earthquakes

At each station we have calculated north- and east-component horizontal-to-horizontal spectral ratios (H/H_{ref}) from the S wave train (Borcherdt, 1970) using the CAP3 and CACH reference sites. Following the procedure described for noise analyses, we have computed the reference spectrum H_{ref}, for the reference sites as the root-mean-square Fourier spectral amplitude from both horizontal components. This procedure is intended to minimize the possible effects of differential response between horizontal components at these sites, isolating the behavior of the site of interest as much as possible from that at the reference site.

The earthquakes have been selected among those recorded simultaneously at the three reference stations and at the array stations, with a satisfactory signal-to-noise ratio (≥ 3) in the frequency band of analysis applying no filtering. Their magnitudes and azimuths are in the ranges $0.8<M_L<2.9$, and 12°-306° respectively (Table 1 and Fig. 3b). The Fourier amplitude spectra have been computed on a window length of 10 s starting from the initial S-wave arrival, which includes the most energetic part of the signal. The selected signals have been processed in similar manner to that previously described for the noise. The signal time-windows have been de-trended and tapered with a Hanning window before being fast Fourier transformed. After applying an arithmetic 0.2 Hz smoothing algorithm to the Fourier amplitude spectra, the spectral ratios have been computed.

We have obtained average spectral ratios subdividing the earthquakes into two groups (group 1: events 4-9-5-6; group 2: events 1-2-3-7-8-10) according to their azimuthal distribution, as described above in the discussion of the reference sites. As previously described, the purpose of this was to highlight possible directional effects, and we found that the spectral ratios for the in-plane and out-of–plane groups of events are remarkably similar in all cases.

Fig. 7 shows the spectral ratios with respect CACH and CAP3 for the selected array stations (from CAB4 to CAO3, see Fig. 3a for their location). The frequency peaks vary from 2.7 Hz to about 4.5 Hz moving downhill from site B4 to site M3. The spectral ratios with respect to CACH have a differential behavior of the N-S and E-W components, with a predominant N-S seismic motion component. This is less evident in the spectral ratios with respect to CAP3, though in both cases the component differences are within standard deviations. Given that the reference H_{ref} is the same for both components, irrespective of the reference site, this difference between the components, if real, must be due to the composition of the wave fields at the array stations. The frequency peaks are much clearer in the area where the slope is less strong, from CAG3 to CAM3. Remembering that the boreholes indicate that MPMU bedrock underlies the array, and CAP3 is on MPMU whereas CACH is on RSU, the average responses with respect to CACH (top panel) have slightly higher amplitude with broader primary and secondary peaks.

While the average responses with respect to CACH and CAP3 are roughly in agreement taking into account the standard deviations, the sizes of the standard deviations are different. Taking CAP3 as the reference results in much smaller standard deviations than using CACH (and, though not shown here, using CAVA gives similar sized but slightly smaller standard deviations to having CACH as the reference). Because CACH is further than CAP3 from the array sites on the landslide (as is CAVA) it could be that at least part of the difference in standard deviation is a consequence of this distance. The 600 m separation of CACH from the array could have lead to differences in the incident wave fields, and possibly also contributions from locally generated waves that are not present at the array, or vice-versa. Furthermore, as we have been stressing, CACH is on a different bedrock unit RSU, which is stratigraphically above the MPMU bedrock below the array and at the other reference sites. Combined with the distance effects, this difference in bedrock is a possible reason for the spectral ratios with respect to CACH having bigger standard deviations than the spectral ratios with respect to CAP3. Under these hypotheses, the apparently higher amplification

level at the array sites on the landslide when CACH is taken as the reference, may be due to properties and behavior at the reference site rather than the actual amplification response of the array sites on the landslide.

Spectral ratios from individual earthquakes

From the 10 earthquakes in Table 1, we have selected four events with sources roughly in line with the profile we use for the 2D simulations and compute spectral ratios separately for each of these earthquakes following the same procedures described before. Events 4 and 9 have back-azimuths of 79° and 71° and reach the array from the northeast, while events 5 and 6 have back-azimuths 246° and 219° from the southwest (Table 1, Fig. 3b). Reference sites CAP3 and CACH have been used in the computation of the individual spectral ratios presented in Figs. 8a-b and 9a-b. In particular, in Fig. 8a-b the top panels show the N-S components and the bottom panels show the E-W components, both using the H_{ref} values from CAP3 (Fig. 8a) and CACH (Fig. 8b).

On one hand, spectral ratios using CAP3 as reference (Fig. 8a) for events 5 and 6 have the N-S components with higher peaks than the E-W components. The exception to this is the high frequency spectral peak between 6 and 7 Hz at station CAM3. Events 4 and 9 do not have such directional behavior. On the other hand, spectral ratios using CACH as reference (Fig. 8b) show opposite behavior, that is the 4 and 9 events have peaks higher than those for the 5 and 6 events though, in this case, the directional behavior of the two components is not as clear as with CAP3 as reference.

Fig. 9a-b shows the radial components (top panel) and the transversal components (bottom panel) for the 4 events, again using the CAP3 (Fig. 9a) and CACH (Fig. 9b) H_{ref} values. We will use these components in the comparison to modeling, comparing SH seismic motion to the transversal components and P-SV seismic motion to the radial components for both reference sites. We notice that not all the sites show a mutually consistent rotation pattern: exceptions are sites CAG3, CAI3 and CAM3, located in the flat area, where a clear association N-S to transversal component appears in all cases regardless of the reference site used.

Modeling and spectral ratios from 2D synthetics

Fig. 3a shows the 2D profile used in the simulations. It has a reference site at both ends, 001, a proxy for CACH, on the southwest side of the landslide, and 086, corresponding to CAP3 on the northeast side, as well as 14 seismometers from the array including CAP3. In the following description we will refer to 001 as CACH and 086 as CAP3.

Landslide thicknesses (Table 2) are an outcome of the multidisciplinary approach used to characterize the Cavola site and integrate geological maps, two refraction lines, the three boreholes, bh1-3, and single-station noise measurements (Bordoni et al., 2007). The geometry of the landslide body along the profile in Fig. 3a for the 2D simulations is between type1 and type 2 according to Bard and Bouchon (1980), with a shape ratio h/D of 0.2 where h = 45 m is the maximum depth to the bedrock and D = 225 m is the half width of the landslide. Using the noise H/V peak frequency, we have refined the bedrock geometry beneath the array computing the thickness of the resonance layer (H), from the standard formula for a normally incident-plane SH wave for a single elastic layer over and elastic half-space: $H = V_s/4f_0$, (Haskell, 1960) where f_0 is the peak frequency and V_s is the average S velocity. Apart from zero at site CAP3, values below the array range from 23 m to 32 m. Elsewhere along the profile single-station noise measurements indicate the greater and more uniform thickness of 45 m. Note that if we had used the frequencies of single peaks fitted to H/H_{ref} from earthquakes, instead of the peaks of the simpler noise H/V spectra, this would have given a greater range of thicknesses below the array, including values close to 45 m at the SW end adjoining the rest of the landslide. We have preferred the use of noise peak frequency to avoid circularity in the comparison of modeling to earthquake observations, though some circularity in the comparison to noise is of course introduced.

Though the model geometry (Fig. 3a) appears very simple with maximum thickness of 45 m, we stress that the real situation is not simply a thin layer over a uniform basement case. Indeed, the bedrock wave velocities measured in the borehole are not characteristic of a proper basement, which must be deeper and must have much higher S velocity. We have not included it in the simulations because we know neither its depth nor its P and S velocities. Furthermore, because of the complex geometry of the formations we expect scattering at the true deeper basement interface to be significant, resulting in waves with a variety of apparent angles of incidence at the base of the landslide. Therefore, though in a thin layer case the

body waves would propagate vertically and the surface waves horizontally, we have preferred to consider several incidence angles as we believe this is more appropriate for the geological setting of the studied area.

As a consequence, we have modeled propagation for SH and SV incident waves at angles of incidence 0°, ±5°, ±10°, ±20°, ±30°, ±45°, ±60°, ±90°, where 0° and 90° are respectively vertical and horizontal incidence, except that ±90 denotes Rayleigh wave incidence in the P-SV case. Seismograms have been generated every 5 m, giving rise to the numbering scheme for the synthetics, though for clarity and to correspond to the spacing in the array only every second trace is plotted in the figures of the seismograms. Here we present 0°, ±20°, ±60°, and ±90°, because ±5° and ±10° have similar properties to 0° and ±20°, whereas ±30° and ±45° are intermediate between those angles and ±60° and ±90°.

Positive incidence angles propagate from the southeast end (left on Fig. 3a) and reach first the CACH site, secondly the array and then the CAP3 site, whereas negative angles propagate from the northeast end (right on Fig. 3a) and reach first the CAP3 site, the array and then CACH. So, for positive propagation CACH is the Front Reference Site (FRS) and CAP3 the Back Reference Site (BRS), while for negative propagation CAP3 is the FRS and CACH is the BRS. This scheme will help us in summarizing ideas in the search for basic rules regarding reference sites.

We have used the impedance-operator-based numerical code developed by Haines and de Hoop (1996). A more approachable description of the mathematical foundations for a geophysical audience is provided by Haines et al., (2004) and Hulme et al., (2004) validate the methodology, showing the power of the approach in comparison with, for instance, the finite difference method. The impedance operator code is formulated in the frequency-wavenumber domain and has many features in common with the reflectivity technique (Kennett, 1983), including its inherent accuracy. The principal advantage over the reflectivity technique is that the impedance operator approach constructs its basic sets of wavefield solutions using matrix additions and multiplications, without the need for the matrix inversions that are necessary in constructing reflection and transmission operators in the reflectivity technique. Consequently, it is much better suited to problems involving lateral heterogeneity which results in coupling between different wavenumbers, though in order to

keep the set of wavenumbers considered at a manageable number the region modeled has to be of limited extent. Fig. 3a shows the full extent of the region considered in the simulations.

The geophysical investigations (Bordoni et al., 2007) have provided us with two velocity-depth models (Table 3): a point measurement at the borehole bh2 and spatially averaged velocities from surface wave analysis. The borehole logging at bh2 indicates a linear gradient in S velocity with no discernable impedance contrast at the contact between the landslide and the underlying MPMU rock, though there is marked change in P wave velocity there. On the contrary, surface wave analysis indicates the presence of an impedance contrast (Bordoni et al., 2007), as do the clear spectral ratio peaks at particularly sites CAG3 and CAI3. So, for simplicity in the simulations we show, we have assumed a constant S velocity of 360 m/s within the landslide that is derived from the surface wave analyses and is also consistent with the average vertical travel time through the landslide at borehole bh2. We have tried a model with a S wave velocity profile without contrast at the bedrock contact as seen in the borehole measurements, but that results in virtually flat spectral ratios across the array in SH simulations, though because of the contrast in P velocity there is better agreement of P-SV simulations with the observations.

As has been outlined, the model geometry is less constrained under station CACH (synthetic site 001) and at other points to the SW of the landslide in Fig. 2. The geological unit outcropping there (RSU) overlies that (MPMU) outcropping at CAP3 reference site and found below the landslide at boreholes bh1 and bh2, but the depth of the interface between the two units SW of the landslide is unknown. The seismic properties of RSU are also unknown. Therefore, to keep our model simple and with few well constrained parameters we have, somewhat arbitrarily, assigned RSU the same properties as MPMU, thereby avoiding the need to guess the shape and depth of the interface between them. In summary, we believe that introducing a complicated geometry at CACH, including properties of RSU that have not been measured, would have detracted from addressing the issues we are investigating.

Comparison between spectral ratios from observations and from modeling

The comparison of synthetics to the spectral ratios sheds light particularly on the issue of choosing the reference for the ratios, and also provides insight into the composition of the observed wavefields (top panels of Figs. 10-13 and Table 4 Supplementary Material).

We have compared synthetic spectral ratios with respect to the synthetic receiver corresponding to CAP3 to the 4 individual events 4-5-6-9 of Table 1 and Fig. 3b, with source back-azimuths in-line with the array. These events have been rotated to the radial and transverse components before computing their spectral ratios (Fig. 9). In particular, spectral ratios for the minus propagation are compared to E-NE source events (4-9) whilst spectral ratios for the plus propagation are compared to W-SW source events (5-6). Note that CAP3 is FRS for the minus propagation direction and is the BRS for the plus propagation (see Fig. 3a). The same scheme has then been applied using the same events and the synthetic receiver corresponding to CACH as reference site, with the obvious difference that CACH is FRS for the plus propagation and BRS for the minus propagation.

We have computed the root mean square misfit between observed and simulated spectral ratios in the following manner:

$$RMS\ misfit = \sqrt{\frac{\sum (Obs_i - Sim_i)^2 \times W_i}{\sum_i W_i}} \qquad (2)$$

where W_i is a weight function with a trapezoidal shape, used here to replace sharp changes in value of the weights from 0 to 1 with gradual changes while focusing on the primary frequency band of amplification in the landslide. So $W_i = 1$ between 2-6 Hz and goes linearly to zero in the frequency bands 0-2 Hz and 6-9 Hz.

In Figs. 10a-b, where CAP3 is the reference site for comparison with earthquake data, the SH for the minus propagation has the lower misfit value (<1) than plus propagation. Specifically, the minus propagation (Fig. 10b) shows a similar misfit trend for all the incidence angles while for the plus propagation (Fig. 10a) a different trend appears for the 0° - 20° and the 60° - 90°, with the former having low misfit comparable to the minus propagation and the latter having almost always misfit value bigger than 1. Therefore, the propagation direction becomes important for incidence angles 60° to 90°: the best match between synthetics and observation is when CAP3 is FRS (Fig. 10b). The P-SV (Fig. 11a-b) is more difficult to interpret. Synthetic seismic motion for angles 0° to 20° again matches data better for the minus propagation (misfit value <=0.6) in comparison to the plus propagation. Near–

horizontal angles (60° to 90°) have better match in the slope area (CAB4 and CAE3) than in the flat area (CAG3, CAI3 and CAM3) for the minus direction of propagation (Fig. 11b).

Using CACH as the reference site, the SH misfit values have the same trend for all incidence angles for the plus propagation (Fig. 12a) while increasing misfit values appear for 60° to 90° in the minus propagation case (Fig. 12b). Because CACH is FRS for the plus propagation, this is a confirmation of patterns with regard to FRS and BRS seen with CAP3 as reference. This can be seen also with P-SV seismic motion. Indeed P-SV misfit values for the plus propagation for 0° 20° and 90° incidence (Fig. 13a) are almost always lower than those for the minus propagation (Fig. 13b) with similar pattern for all the angles. An exception is the +60° incidence angles with misfit values bigger than 3.

Therefore, using a FRS appears to be the best choice for evaluating the true seismic response of the landslide. On this basis, the directional effect described in Figs. 8-9 appears as an effect of the BRS instead of the proper response of the landslide. We discuss this issue more in the next section.

As regard to the seismic wavefield at the landslide, although the SH provides in general lower misfit than P-SV, we cannot quantify the role of in-plane and out-of-plane seismic motions which both appear to contribute to the wavefield there. This is true for CACH and CAP3 as reference, though the misfit values are always higher (especially for SH) for CACH. The likely reason for this difference between the two reference sites is the simplification in the modeling we did, assuming that the RSU bedrock under CACH has the same elastic properties as the fractured MPMU under CAP3.

Discussion

The effect of direction of propagation and reference site location

We have observed that a FRS performs better than a BRS one. Here we will show in detail why this happens. Fig. 14 shows Fourier amplitude spectra at receivers 086 and 001, corresponding to CAP3 and CACH, for SH (top) and P-SV (bottom), minus and plus seismic motion simulations (left and right respectively in Fig. 14). For both directions of propagation of SH, if the two reference sites are BRS their amplitude spectra are de-amplified over the

entire frequency range in comparison to when they are FRS (Fig. 14 top panel), possibly as a result of partial shadow zones forming behind the landslide. For P-SV differences appear between the two directions of propagations: for minus propagation the BRS is amplified for frequencies less than 3 Hz in comparison to the FRS (Fig. 14 bottom left panel) whereas for plus propagation the BRS is strongly amplified for frequency higher than 2 Hz (Fig. 14 bottom right panel) in comparison to the FRS. This P-SV behavior suggests likely focusing of energy in particular frequency bands behind the landslide, with the difference between the two directions reflecting differences in shape at the two ends of the landslide for the profile in Fig. 3a. We confirm these interpretations by examining the corresponding synthetic seismograms.

We present three figures showing SH and P-SV synthetics for incidence angles of 20° and 60° (Figs. 15-17). In particular, the vertical component U_z as well as the horizontal component U_x are presented for the P-SV seismic motion synthetics with SV waves incidence angle of 60°. SH calculations were performed up to 18.75 Hz, whereas the P-SV calculations were performed up to 9.375 Hz. The incident waveform used for both wavefields is a Gabor function with the analytical form:

$$f(t) = \exp\left[\frac{-\omega_p (t - t_S)}{\gamma^2}\right] \cos\left[\omega_p (t - t_S) + \psi\right] \qquad (3)$$

where: $\omega_p = 2\pi f_p$ *and* $t_S = \frac{0.45\gamma}{f_p}$.

The values of γ=0.24, $\psi = \frac{\pi}{2}$, and $f_p = 0.45Hz$. This was altered by a factor of 2 in frequency between the two cases to correspond to the frequency ranges over which the synthetics were calculated. Because of their higher frequency content, the SH synthetics show the individual waves traveling within the landslide somewhat better. On the other hand, spectral ratios (Figs. 10-13) show that the P-SV simulations do not have less amplification than SH in the frequency band of interest (0-9 Hz).

Synthetics for the plus and minus directions of propagation are shown together. Looking first at the SH examples, the ±60° results (Fig. 15) show more asymmetric patterns of waves diffracted from the two ends of the landslide than the ±20° results (Fig. 16 top panels). The

±60° (Fig. 15) result shows much stronger diffractions from the front end with respect to the incident wave than from the back end. The first arrivals are the incident SH waves, which are refracted at the base of the landslide and transmitted through the landslide body. Others wave trains are diffracted by the NE and the SW bottom corners of the landslide, and also by the little bump in the basement topography beneath the array. It is also possible to note later reflections of the diffracted waves traveling horizontally inside the landslide with the 360 m/s S wave speed there (left-hand side of Fig. 15, minus propagation). Many such arrivals are visible in the later part of the time series, and in Fig. 15 there is a strong hint of a head wave with higher apparent velocity that has traveled along the top of the basement below the landslide for the minus direction of propagation (left-hand side of Fig. 15, minus propagation). These synthetics also show the effect of direction of propagation on the reference sites. For ±20° (Fig. 16 top panels) there are slight differences between the bedrock responses at the two ends of the landslide, while differences appear clearly for the incidence angles ± 60° (Fig. 15). The FRS is illuminated before the landslide and preserves the wave contents of the incident wave, whereas for SH the BRF has diminished amplitude of the incident wave and later arrivals are also small in amplitude.

For P-SV this pattern is altered through the contributions of two effects. First, there appears to be a greater degree of leakage of energy from within the landslide to the BRF than for SH. This is likely in part due to the low impedance contrast between the landslide and the basement (such as demonstrated by Bard and Bouchon, 1980). Second, there is complicated behavior associated with changes in the direction of ground motion. For ±60° the incident SV wave involves predominantly vertical motion (Fig. 17 bottom panels), and this feature is preserved at the FRS. On entering the landslide body the refracted S wave has much more horizontal particle motion, and the greater proportion of horizontal motion is imparted to the BRF (Fig. 17 top panels). The differences between FRS and BRF for P-SV, as for SH, are much slighter for ±20° incidence (Fig. 16 bottom panel) than for ±60°.

Using a flat half-space reference model and comparison with noise spectral ratios

Flat Half-Space Reference Models (FHSRM, which are 1D in the sense of having a free surface, and 0D otherwise) are arguably the most convenient for synthetic calculations and also the best in an absolute sense. The P-SV synthetics for ±20° and ±60° (Fig. 16 bottom; Fig.17) illustrate the root cause of a problem in calculating either standard H/V or H/H

spectral ratios from results of simulations. For near vertical angles of incidence such as ±20° the vertical component is negligible in comparison with the horizontal component (and we do not show it), and is of course identically zero in the case of SH waves. Consequently, it is not sensible to calculate H/V spectral ratios. For more horizontal incidence of SV waves the vertical component is the dominant component at FRS (Fig. 17 bottom panel), and in the special case of 45° incidence in flat topography the horizontal component is zero at the surface because the horizontal components of the incident wave and the surface reflection cancel exactly there, whereas the vertical components have the same signs and constructively combine. Thus, for such angles in the P-SV case the value of calculating H/H spectral ratios is also questionable. The obvious and logical compromise to obtain a fully robust spectral ratio for P-SV for all angles of incidence is to use as denominator either the largest component or the largest multi-component polarization (constructed by combining the maximum horizontal and vertical components) as the bedrock reference.

The use of such a reference for modeled spectral ratios in comparing them with observed spectral ratios requires the reference for the observed spectral ratios to be an absolute reference as well. The vertical component in noise measurements is close to an absolute reference. Therefore in the comparison with H/V from noise we have computed the spectral ratio from the simulations between the horizontal component in the 2D simulation (as usual) and the maximum combined horizontal and vertical polarization at the surface in the FHSRM. The latter has the same properties as the basement in the 2D simulation. We have called this ratio H/M.

Fig. 18 shows results for the SH simulations, for which the reference site is simply the out-of-plane horizontal component in the FHSRM for the plus (Fig. 18a) and minus (Fig. 18b) propagation. The agreement is very good with observed noise H/V spectral ratios, which in turn agree quite well with the $H/H_{\mathbf{ref}}$ spectral ratios from earthquakes with CAP3 as the reference site (compare Fig. 5 and Fig. 7, bottom panel). There is some circularity in this as the noise spectral ratios were used to deduce the landslide thickness for the simulations, based on the standard formula for vertically propagating SH waves.
Fig. 19 shows results for the P-SV simulations, where a good level of fit is obtained both for plus (19a) and minus (19b) propagation, for virtually all angles of incidence.

As a consequence of the FHSRM being independent of contributions specific to the BRS and FRS, the misfit values are similar for plus and minus propagation, and for P-SV as well as SH. This comparison stresses the role of using the appropriate reference site, whose response can be influenced by the propagation as already shown by Figs. 10-13.

As regard to the seismic wavefield in the landslide, because misfits are good for both SH and P-SV wavefields, we do not obtain information from this comparison about the composition of the noise wavefield, other than that it could be made up of waves with pretty much any angle of incidence at the base of the landslide, though clearly it cannot be purely SH waves as there has to be some vertical component motion.

Potential and limits of 1D simulation

The last issue we address is what extent can 1D models also be used at the landslide sites to obtain satisfactory spectral ratios. This is a topic that has received a lot of attention in the literature, notably in the seminal work of Bard and Bouchon (1985). They classify sedimentary basins according to whether the response is likely to be 1D or 2D. Our case is intermediate with a shape ratio h/D of 0.2.

In Fig. 20a-b we compare 1D modeling results, using the structure in Fig. 3b vertically below each of the array sites (see Table 2), to the spectral ratios from our 2D simulations with CAP3 as the reference site. This is done for incidence angles of 0°, 30° and 60°. For SH (Fig. 20a) the agreement for the vertical incidence and for the 30° minus propagation appear fairly good with a match to the first peak at each of the landslide sites both in terms of amplitude and frequency, the latter with a variation of ±0.5 Hz. There is no match for angles of incidence of 30° plus propagation and for 60° (both direction of propagation). The corresponding results for P-SV (Fig. 20b) are much the same, except that for vertical incidence the mismatch in peak frequencies is greater, with about 1 Hz differences and that this time is the 30° plus propagation to fit better that data at some stations. We conclude that even for vertical incidence 1D simulation cannot be used as an accurate proxy for 2D simulation in our situation, in accord with the general inference of Chàvez-Garcìa (2003).

Conclusions

In this paper we have investigated issues related to the direction of propagation of wave fronts in relation to the relative positions of a reference site and the site of interest. Our study is based on comparison of spectral ratios from observation (earthquakes and noise) and 2D numerical simulations for SH and P-SV seismic motion propagating into the model from its two opposite ends for a comprehensive set of incidence angles (0° to 90°).

A feature of our study has been having three bedrock reference sites, with one being part of the seismograph array on the Cavola landslide (Bordoni et al. 2007). That reference site CAP3 gives spectral ratios from earthquakes with much smaller standard deviations than the other two reference sites CACH and CAVA (for results with CAVA as the reference site see the Supplementary figures). CACH, which gives the largest standard deviations, is on a different bedrock unit RSU than the MPMU bedrock underlying the landslide at the array, whereas CAP3 and CAVA are on MPMU. The average spectral ratios are different for the three references, but there is general agreement when standard deviations are taken into account.

Comparing 2D synthetic calculations with the earthquake observations we get good agreement for SH, particularly for near vertical incidence, and also for near horizontal incidence with a reference site on the same side of the landslide as the incoming waves. The fit is slightly less good for P-SV but with some features of the observations matched. Both CAP3 and CACH are inline with our 2D modeling profile. With CACH as the reference the match is broadly similar in its trends to when CAP3 is the reference, but the actual misfits are not as good as with CAP3. We believe much of the misfit with CACH as reference can be attributed to CACH being on different bedrock (RSU) to the highly fractured bedrock (MPMU) under the array and at CAP3. At the same time we believe too little is known about the bedrock under CACH for it to have been convincingly included in the modeling.

The key conclusion of this paper is the difference between Front Reference Site (FRS) and Back Reference Site (BRS). A FRS is on the same side of the non-basement deposits as the source and receives the incident waves without being strongly affected by interaction of the waves with the landslide body in our case. In contrast, a BRF is on the opposite side of the landslide to the epicenters and is strongly affected by such interactions. This is particularly noticeable for SH waves. We have shown in our modeling that for SH waves BRF tend to be

in shadow zones, resulting in significant reduction in the spectral amplitude of the wavefield there. Consequently, when a BRF is used in calculating spectral ratios the spectral ratios tend to be over-estimates of the real situation. This conclusion can be applied to cases where heterogeneous low density surface bodies make possible the presence of shadow zones.

Acknowledgements

P.B. thanks Marco Cattaneo, Alessandro Amato, and Giovanna Cultrera, from INGV, who believed in the '100 seismometers project' from the beginning and helped in making it happen. P.B. acknowledges Salvatore Mazza, from INGV, for guidance in writing shell scripts. We all thank NERC SEIS-UK for use of their equipment, and Anna Horleston and Alex Brisbourne from SEIS-UK for their invaluable help in the field. We have used SAC2000 (Goldstein et al. 2003) for data processing. The (i) Area Ambiente e Sviluppo Sostenibile of Provincia di Modena, (ii) Area Pianificazione e Tutela del Territorio of Provincia di Reggio Emilia, (iii) Servizio Tecnico of Comune di Toano, (iv) Servizio Geologico, Sismico e dei Suoli of Regione Emilia Romagna provided funding and logistic support for the project, and Mr Monticelli kindly allowed us to deploy the seismograph array in his field. Last but not least, we are very grateful to the Reviewers and Associate Editor for their insightful comments and knowledgeable guidance in improving the paper.

References

Abercrombie, R. E., (1997). Near-surface attenuation and site effects from comparison of surface and deep borehole recordings, *Bull. Seism. Soc. Am.* **87** 731-744.

Bard, P.-Y., and M. Bouchon (1980). The seismic response of sediment-filled valleys. Part II. The case of incident P and SV waves, *Bull. Seism. Soc. Am.* **70** 1921-1941.

Bard, P.-Y., and M. Bouchon (1985). The two-dimensional resonance of sediment-filled valleys, *Bull. Seism. Soc. Am.* **75** 519-541.

Bertolini, G. and M. Pellegrini (2001). The landslides of the Emilia Apennines (Northern Italy), with reference to those which resumed activity in the 1994-1999 period and required Civil Protection interventions*, Quad. Geol. Appl*. **8** 27-74.

Bertolini, G., and M. Pizziolo (2008). Risk assessment strategies for the reactivation of earth flows in the Northern Apennines (Italy), *Eng. Geol.* **102** 178-192.

Bonnefoy-Claudet, S., A. Köhler, C. Cornou, M. Wathelet, and P.Y. Bard (2008), Effects of Love waves on microtremor H/V ratio. Bull. Seism. Soc. Am., 98 (1), 288-300.

Borcherdt, R. D. (1970). Effects of local geology on ground motion near San Francisco Bay, *Bull. Seism. Soc. Am.* **60** 29–61.

Bordoni, P., J. Haines, G. Di Giulio, G. Milana, P. Augliera, M. Cercato, L. Martelli, F. Cara, and the Cavola Experiment Team (2007). Cavola experiment site: geophysical investigations and deployment of a dense seismic array on a landslide, *Ann. of Geophys.* **50** 627-649.

Bordoni, P., F. Cara, G. Di Giulio, A.J. Haines, G. Milana, and A. Rovelli (2009). Seismic response and wavefield characterization using a very dense 2D seismic array on an active landslide (Cavola, Italy), *SSA Annual Meeting 8-10 April*, 2009 Monterey, California.

Brunamonte, F. (1999). *Catalogo Frane Storiche Provincia di Reggio Emilia (cat-re1.0)*. CNR-IRPI Torino.

Cara, F., G. Di Giulio, G. Milana, P. Bordoni, J. Haines and A. Rovelli (2009). On the stability and reproducibility of the horizontal-to-vertical spectral ratios on ambient noise: the case study of Cavola, northern Italy, submitted to *Bull. Seism. Soc. Am.*

Castello, B., G. Selvaggi, C. Chiarabba, and A. Amato (2006). CSI Catalogo della sismicità italiana 1981-2002, versione 1.1. INGV-CNT, Roma, url: http://www.ingv.it/CSI/

Chàvez-Garcìa, F. J. (2003). Site effect in Parkway basin: comparison between observations and 3-D modeling, *Geophys. J. Int*. **154** 633-646.

Frischknecht, C., and J. J. Wagner (2004). Seismic Soil Effect in an Embanked Deep Alpine Valley: A Numerical Investigation of Two-Dimensional Resonance, *Bull. Seism. Soc. Am.* **94** 171-186.

Goldstein, P., D. Dodge, M. Firpo, and L. Minner (2003). *SAC2000: Signal processing and analysis tools for seismologists and engineers, Invited contribution to 'The IASPEI International Handbook of Earthquake and Engineering Seismology',* Edited by WHK Lee, H. Kanamori, P.C. Jennings, and C. Kisslinger, Academic Press, London.

Gruppo di lavoro CPTI (2004). *Catalogo Parametrico dei Terremoti Italiani, versione 2004 (CPTI04),* INGV, Bologna. http://emidius.mi.ingv.it/CPTI04/

Haines, A.J., and M.V. de Hoop (1996). An invariant bedding analysis of general scattering problems, *J. Math. Phys.* **37** 3854-3881.

Haines, A. J., T. Hulme, and J. Yu (2004). General elastic wave scattering problems using an impedance operator approach – I. Mathematical development, *Geophys. J. Int.* **159** 643-657.

Haskell, N. A. (1960). Crustal reflection of plane *SH* waves, *J. Geophys. Res*. **65**, 4147-4150.

Hulme, T., Haines, A. J., and J. Yu (2004). General elastic wave scattering problems using an impedance operator approach – II. Two-dimensional isotropic validation and examples, *Geophys. J. Int.* **159** 658-666.

Kennett, B.L.N. (1983). *Seismic wave propagation in stratified media*, Cambridge University Press, Cambridge.

Mancin, N., L. Martelli and C. Barbieri (2006). Foraminiferal biostratigraphic and paleobathymetric constraints in geohistory analysis: the example of the Epiligurian succession of the Secchia Valley (Northern Apennines, Mid Eocene-Late Miocene). *Boll. Soc. Geol. It.* **125** 163- 186.

Nakamura, Y. (1989). A method for dynamic characteristics estimation of subsurface using microtremors and the ground surface. *Quarterly Rept. RTRI Japan* 30, 25-33.

Plesi, G. (2002). Carta Geologia d'Italia alla scala 1:50,000, Foglio 235 "Pievepelago". Servizio Geologico d'Italia, Regione Emilia-Romagna, Servizio Geologico, Sismico e dei Suoli, Selca, Firenze

Steidl, J. H., A. G. Tumarkin, and R. J. Archuleta (1996). What is a reference site? *Bull. Seism. Soc. Am.* **86** 1733-1748.

Authors' affiliations, addresses

Giuseppe Di Giulio
Istituto Nazionale di Geofisica e Vulcanologia, sezione Roma 1
Via di Vigna Murata 605
00143 Roma, Italy.

Alan John Haines
Institute of Geological and Nuclear Sciences Limited (GNS Science)
764 Cumberland Street
Dunedin 9016, Otago, New Zealand

Fabrizio Cara
Istituto Nazionale di Geofisica e Vulcanologia, sezione Roma 1
Via di Vigna Murata 605
00143 Roma, Italy.

Giuliano Milana
Istituto Nazionale di Geofisica e Vulcanologia, sezione Roma 1
Via di Vigna Murata 605
00143 Roma, Italy.

Antonio Rovelli
Istituto Nazionale di Geofisica e Vulcanologia, sezione Roma 1
Via di Vigna Murata 605
00143 Roma, Italy.

Tables

Table 1: Earthquake hypocenter parameters.

Code	Date	Time	Lat	Lon	BAZ	Dist	Ml	Num
04212005732	30/7/04	005732	44.221	10.620	159	21	1.9	1
04219062852	06/8/04	062852	44.435	10.518	348	5	1.1	2
04224001007	11/8/04	001007	44.424	10.526	355	3	1.4	3
04224001104	11/8/04	001104	44.404	10.591	79	3	0.8	4
04227122205	14/8/04	122205	44.287	10.215	246	30	2.1	5
04263042200	19/9/04	042200	44.165	10.273	219	30	1.7	6
04265105043	21/9/04	105043	44.980	9.358	306	114	2.9	7
04267173958	23/9/04	173958	44.511	10.565	12	12	1.2	8
04272070852	28/9/04	070852	44.425	10.610	71	6	1.9	9
04274204331	30/9/04	204331	44.240	10.510	185	18	2.5	10

Table 2: Thickness of landslide from Noise H/V.

Site	Peak F0 (Hz)	Thickness (m)
A3	2.8	32
B3	2.9	32
C3	2.9	31
D3	2.9	32
E3	3.4	27
F3	3.4	26
G3	3.4	26
H3	3.6	25
I3	3.7	24
L3	3.8	24
M3	3.8	24
N3	3.9	23
O3	3.9	23

Table 3: Velocity-depth profiles at borehole bh2.

Model	Layer	Thickness (m)	Density (gm/cm^3)	V (m/s)	Qs	P (m/s)	Qp
Linear Model	1	3	1.9	230	0.05	520	0.025
	2	22	1.9	300	0.05	1630	0.025
	Half-space	-	2.0	625	0	2850	0
Constant Model	1	25	1.9	360	0.05	1500	0.025
	Half-space	-	2.0	800	0	3000	0

Figure Captions

Fig. 1: Study area: sketch map of the Cavola landslide body in relation to geology

Fig. 2: Detail of the geology at Cavola village including basement and landslide geology. The black dashed line is the trace of the profile for the 2D modeling, with the indication of boreholes. CAP3, CAVA and CACH are the reference sites. In the upper panel, details are shown concerning location of boreholes, geophysical measurements, and layout of the seismic array.

Fig. 3: a) model used in the 2D numerical simulation, with direction of propagation sign conventions, location of the seismographs used for comparison to modeling and the boreholes (black columns); b) earthquake locations.

Fig. 4: Example of recording, for earthquake 5 in Table 1; a) band pass filtered between 0.8 and 5 Hz, East component (top panel) and North component (bottom panel); b) band pass filtered between 5 and 10 Hz, East component (top panel) and North component (bottom panel).

Fig. 5: Noise spectral ratios, with comparison between horizontal-to-vertical and horizontal-to-horizontal using CAP3 reference site (top panel), and CACH reference site (bottom panel).

Fig. 6: Spectral properties of the three reference sites. The top panels are the H/V spectral ratios using ambient noise: they show a substantially flat behavior. The other panels show the SSR between the different reference sites. Group 1 and 2 include events that strike the array in-plane and out-of-plane, respectively.

Fig. 7: Earthquake spectral ratio averages, and ± one standard deviation, computed using CACH reference site (top) and CAP3 reference site (bottom). Group 1 and 2 include events that strike the array in-plane and out-of-plane, respectively. Each reference site spectrum is computed as the root-mean-square Fourier amplitude from both horizontal components.

Fig. 8a: Earthquake spectral ratios for events 5,6,7,9 from Table 1, using CAP3 as reference site; (top panel) North component, (bottom panel) East component.

Fig. 8b: As Fig. 8a, using CACH as reference site.

Fig. 9a: Earthquake spectral ratios for events 5,6,7,9 from Table 1, using CAP3 as reference site; (top panel) Radial component, (bottom panel) Transversal component.

Fig. 9b: As Fig. 8a using CACH as reference site.

Fig. 10a: (Top panels) H/H synthetics of SH simulation with site 086 as reference versus individual earthquake spectral ratios using CAP3 as reference site. Incidence angles of simulations are 0°, 20°, 60°, 90°. Source back-azimuth is W-SW (plus propagation). (Bottom panels) Misfit between observed and synthetics spectral ratios for different models and events.

Fig. 10b: As Fig. 10a, for source back-azimuth E-NE (minus propagation).

Fig. 11a: (Top panels) H/H synthetics of P-SV simulation with site 086 as reference versus individual earthquake spectral ratios using CAP3 as reference site. Incidence angles of simulations are 0°, 20°, 60°, 90°. Source back-azimuth is W-SW (plus propagation). (Bottom panels) Misfit between observed and synthetics spectral ratios for different models and events.

Fig. 11b: As Fig. 11a, for source back-azimuth E-NE (minus propagation).

Fig. 12a: (Top panels) H/H synthetics of SH simulation with site 001 as reference versus individual earthquake spectral ratios using CACH as reference site. Incidence angles of simulations are 0°, 20°, 60°, 90°. Source back-azimuth is W-SW (plus propagation). (Bottom panels) Misfit between observed and synthetics spectral ratios for different models and events.

Fig. 12b: As Fig. 12a, for source back-azimuth E-NE (minus propagation).

Fig. 13a: (Top panels) H/H synthetics of P-SV simulation with site 001 as reference versus individual earthquake spectral ratios using CACH as reference site. Incidence angles of

simulations are 0°, 20°, 60°, 90°. Source back-azimuth is W-SW (plus propagation). (Bottom panels) Misfit between observed and synthetics spectral ratios for different models and events.

Fig. 13b: As Fig. 13a, for source back-azimuth E-NE (minus propagation).

Fig. 14: Fourier Amplitude Spectra of SH (top panel) and P-SV (bottom panel) seismic motion simulations at receivers corresponding to reference sites CAP3 (086) and CACH (001). The incidence angle is ±60°. Black and grey curves correspond to 086 and 001 reference sites respectively.

Fig. 15: Synthetics seismograms for SH ±60° incidence.

Fig. 16: Synthetics seismograms for a) SH ±20° incidence, b) horizontal component for SV ±20° incidence

Fig. 17: Synthetics seismograms for a) horizontal component for SV ±60° incidence, b) vertical component for SV ±60° incidence

Fig. 18a: (Top panels) H/M synthetics with corresponding flat half-space as reference for SH versus noise H/V spectral ratios. Incidence angles of simulations are 0°, 20°, 60°, 90° with source back-azimuth W-SW (plus propagation). (Bottom panels) Misfit between observed and synthetics spectral ratios for different models and events.

Fig. 18b: As Fig. 18a, for source back-azimuth E-NE (minus propagation).

Fig. 19a: (Top panels) H/M synthetics with corresponding flat half-space as reference for P-SV simulations versus noise H/V spectral ratios. Incidence angles of simulations are 0°, 20°, 60°, 90° with source back-azimuth W-SW (plus propagation). (Bottom panels) Misfit between observed and synthetics spectral ratios for different models and events.

Fig. 19b: As Fig. 19a, for source back-azimuth E-NE (minus propagation).

Fig. 20: Comparison between spectral ratios from 1D and 2D a) SH simulations for incidence angles of 0°, 30° and 60°; b) P-SV simulations for incidence angles of 0°, 30° and 60°.

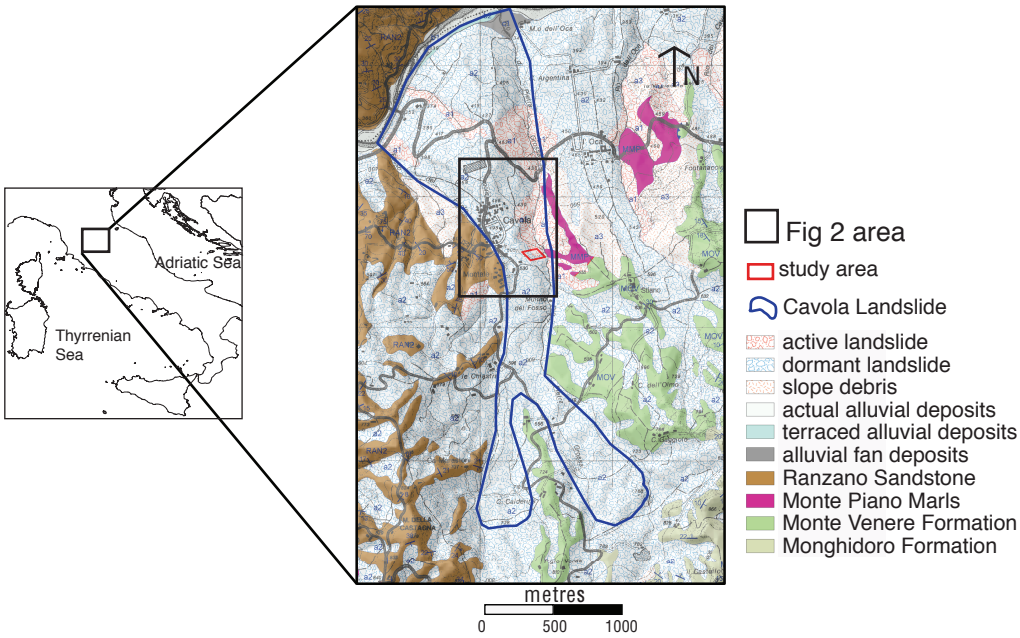
Adriatic Sea
Thyrrenian Sea
N
Fig 2 area
study area
Cavola Landslide
active landslide
dormant landslide
slope debris
actual alluvial deposits
terraced alluvial deposits
alluvial fan deposits
Ranzano Sandstone
Monte Piano Marls
Monte Venere Formation
Monghidoro Formation
metres
0
500
1000

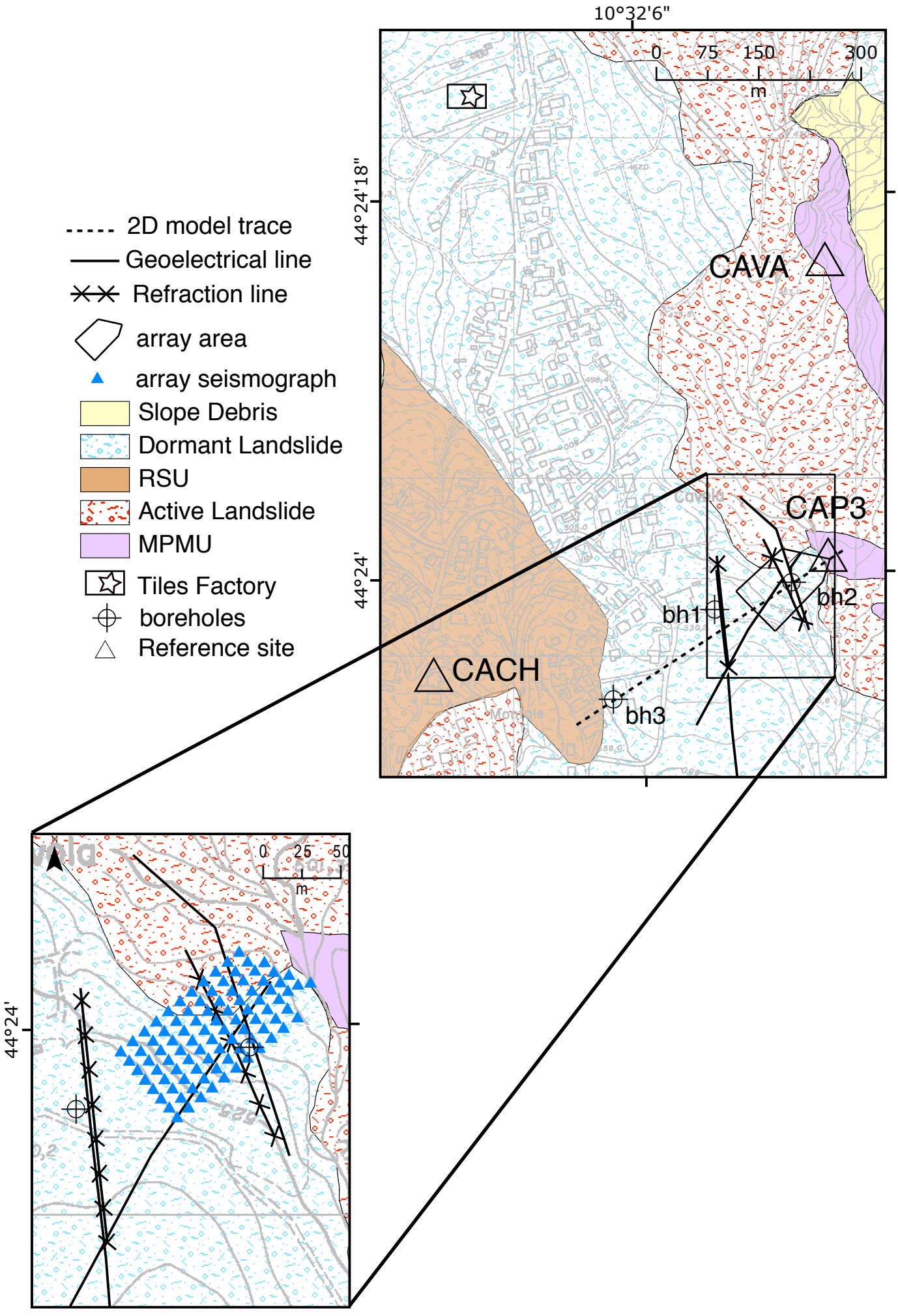
10°32'6"
44°24'18"
44°24'
0 75 150 300
m
CAVA
CAP3
bh1
bh2
bh3
CACH
0 25 50
m
44°24'
2D model trace
Geoelectrical line
Refraction line
array area
array seismograph
Slope Debris
Dormant Landslide
RSU
Active Landslide
MPMU
Tiles Factory
boreholes
Reference site

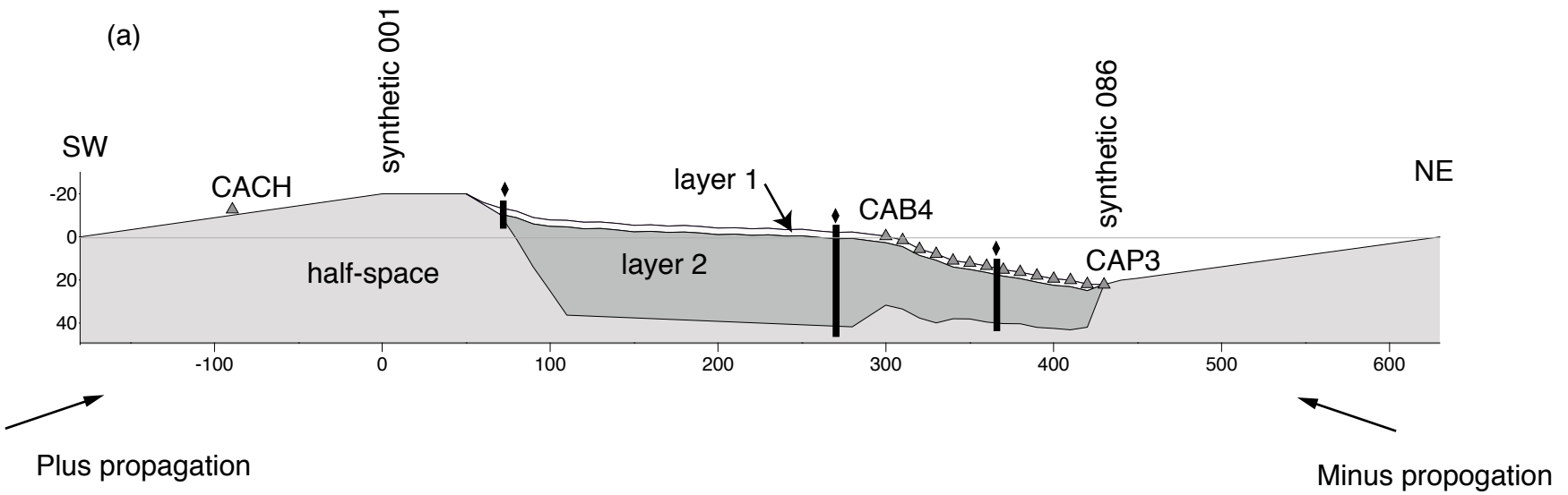
(a)
synthetic 001
synthetic 086
SW
NE
CACH
layer 1
CAB4
CAP3
half-space
layer 2
-20
0
20
40
-100
0
100
200
300
400
500
600
Plus propagation
Minus propogation

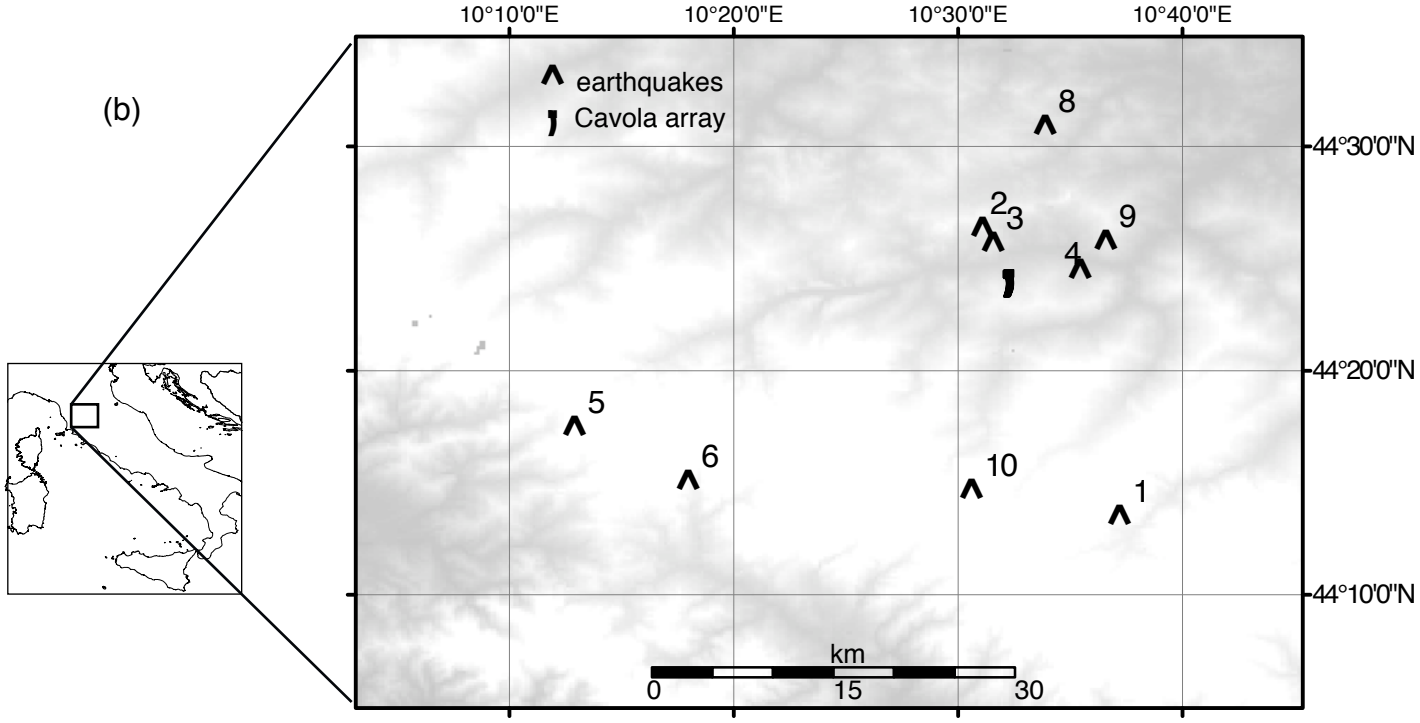
(b)
10°10'0"E
10°20'0"E
10°30'0"E
10°40'0"E
earthquakes
Cavola array
44°30'0"N
44°20'0"N
44°10'0"N
km
0
15
30

North component, band pass filtered between 0.8 - 5 Hz

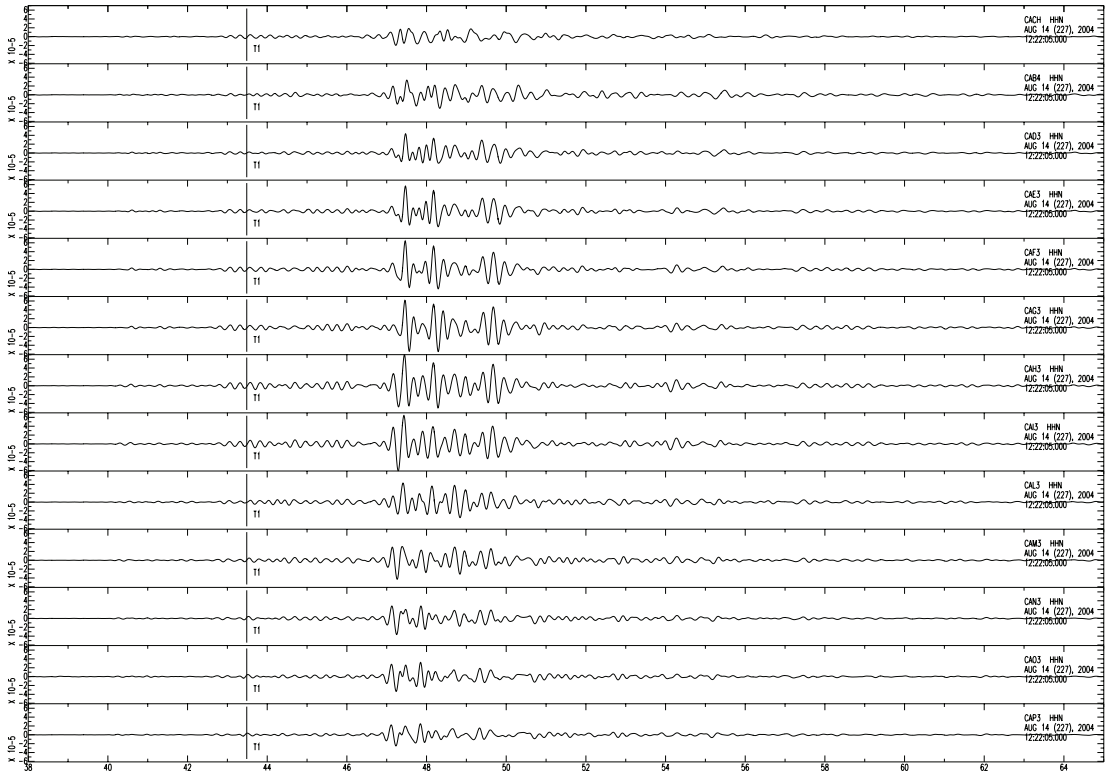

East component, band pass filtered between 0.8 - 5 Hz

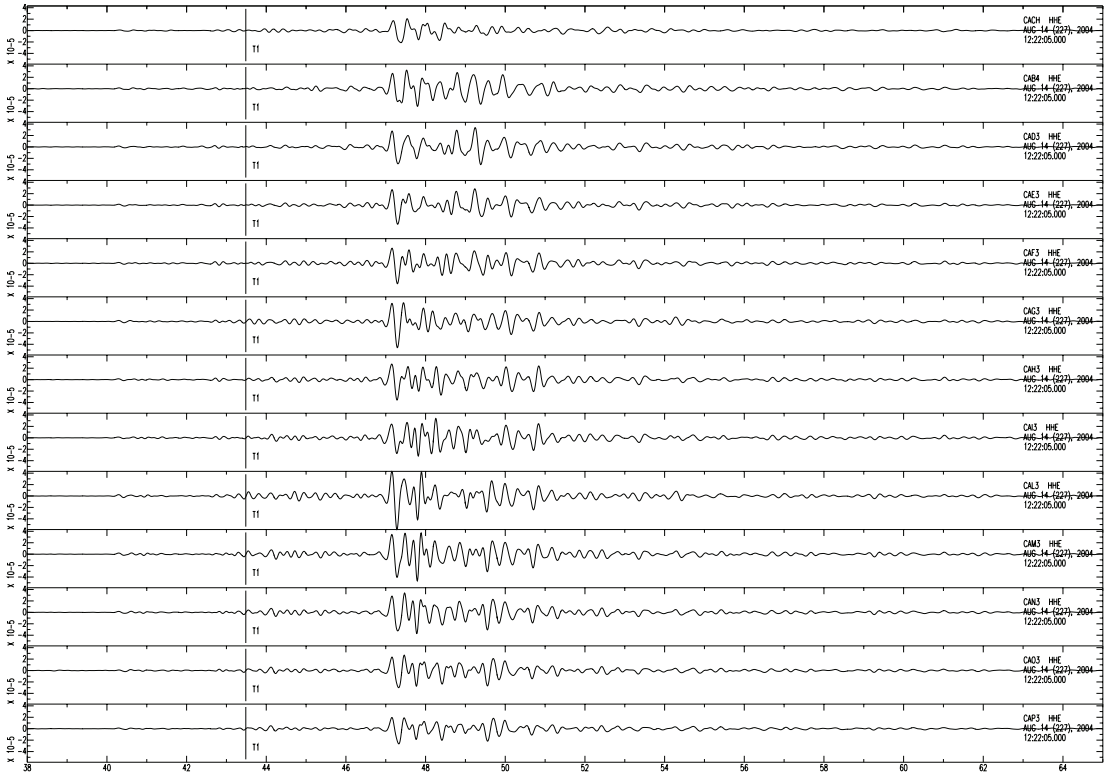

6 x10^{-5} m/s

10 s

North component, band pass filtered between 5 - 10 Hz

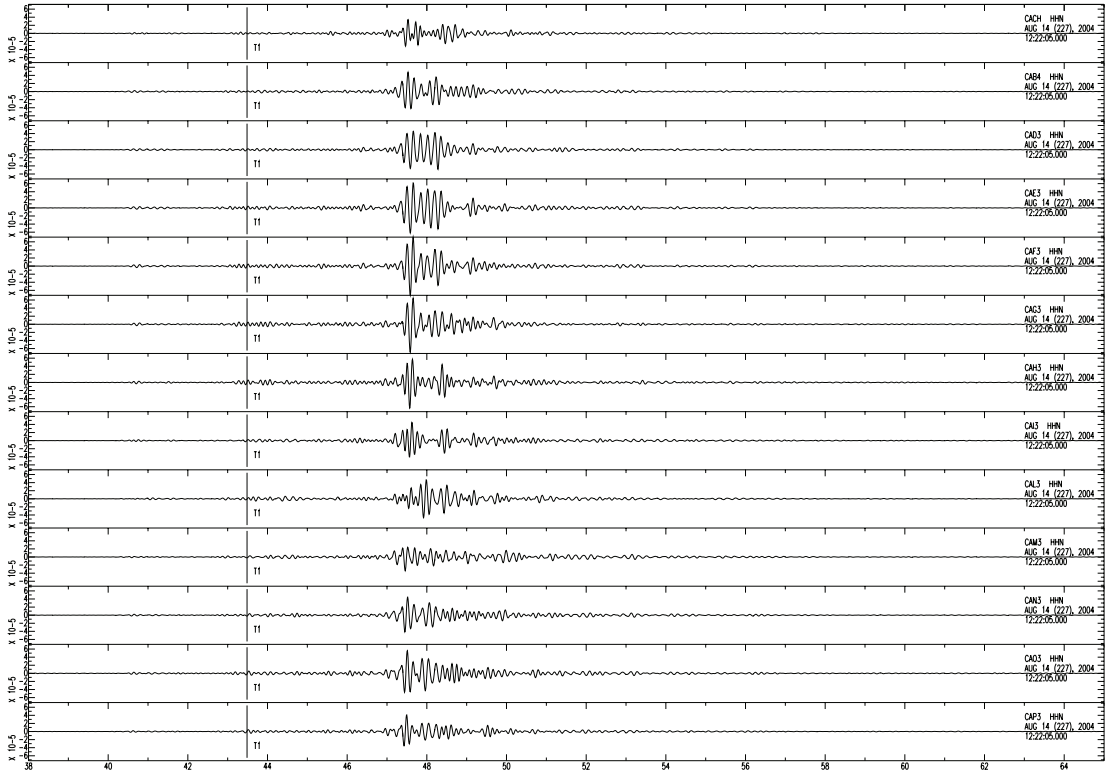

East component, band pass filtered between 5 -10 Hz

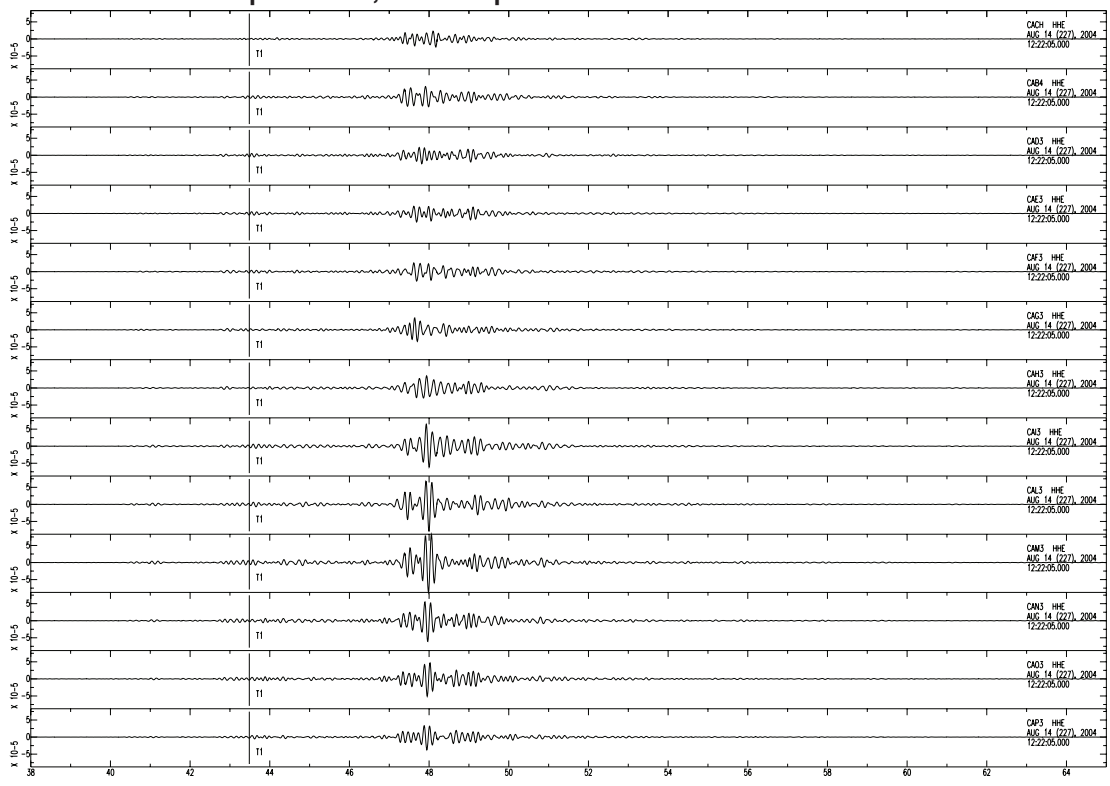

6 x10^{-5} m/s

10 s

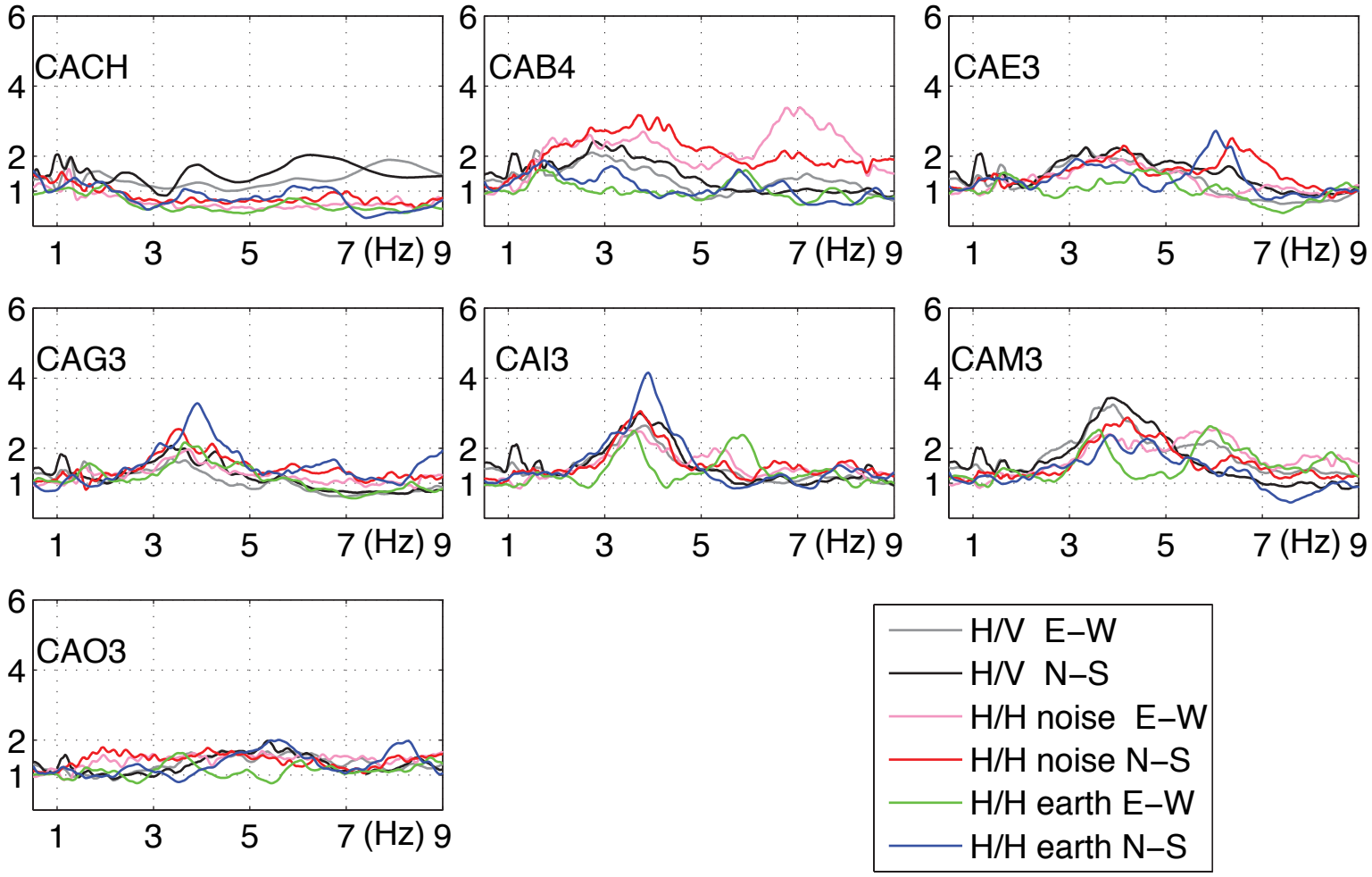
a) H/V, H/H CAP3 NOISE N/H events CAP3
CACH
CAB4
CAE3
CAG3
CAI3
CAM3
CAO3
6
4
2
1
1 3 5 7 (Hz) 9
H/V E–W
H/V N–S
H/H noise E–W
H/H noise N–S
H/H earth E–W
H/H earth N–S

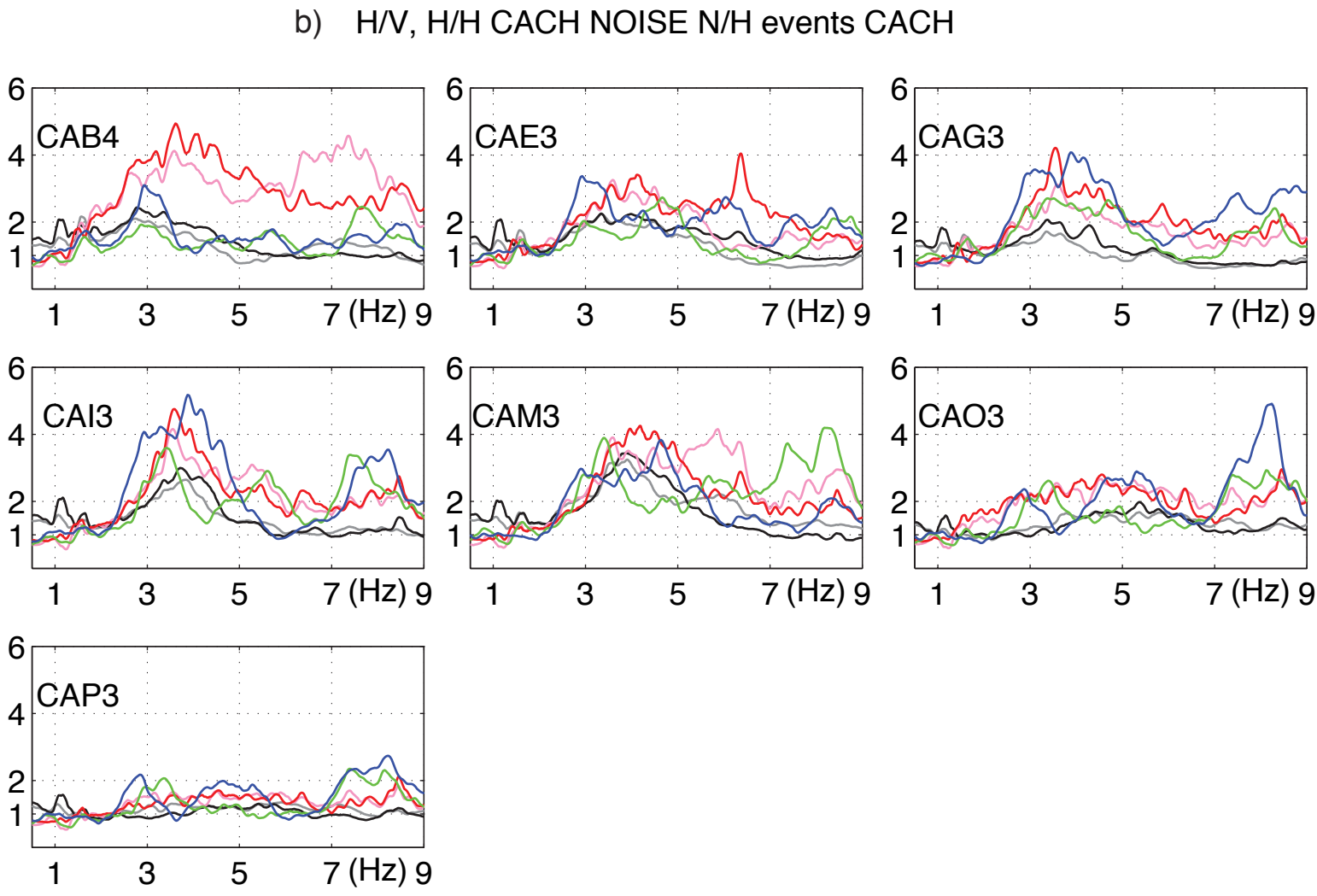
b) H/V, H/H CACH NOISE N/H events CACH
CAB4
CAE3
CAG3
CAI3
CAM3
CAO3
CAP3
6
4
2
1
1 3 5 7 (Hz) 9

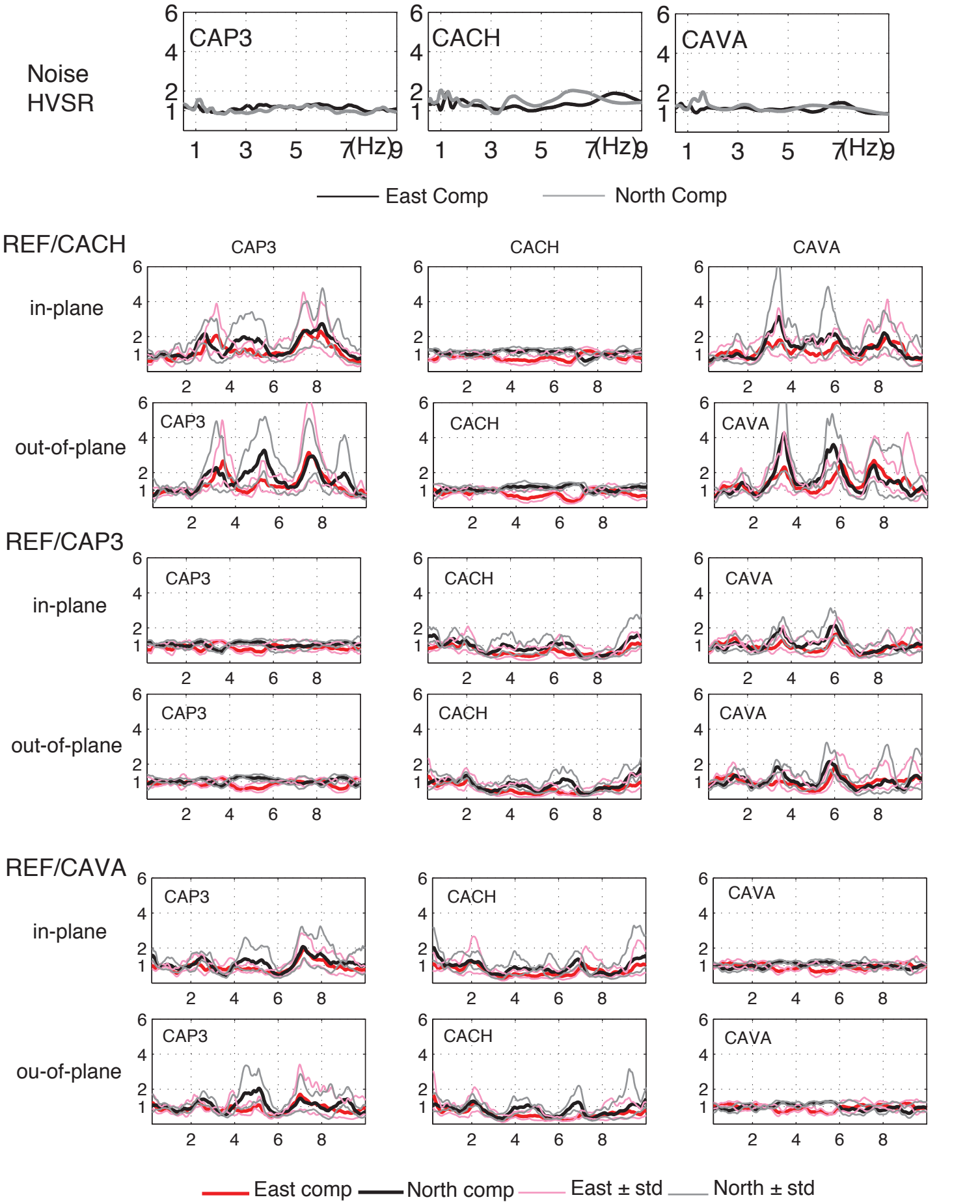
Noise
HVSR
CAP3
CACH
CAVA
(Hz)
East Comp
North Comp
REF/CACH
REF/CAP3
REF/CAVA
in-plane
out-of-plane
ou-of-plane
East comp
North comp
East ± std
North ± std

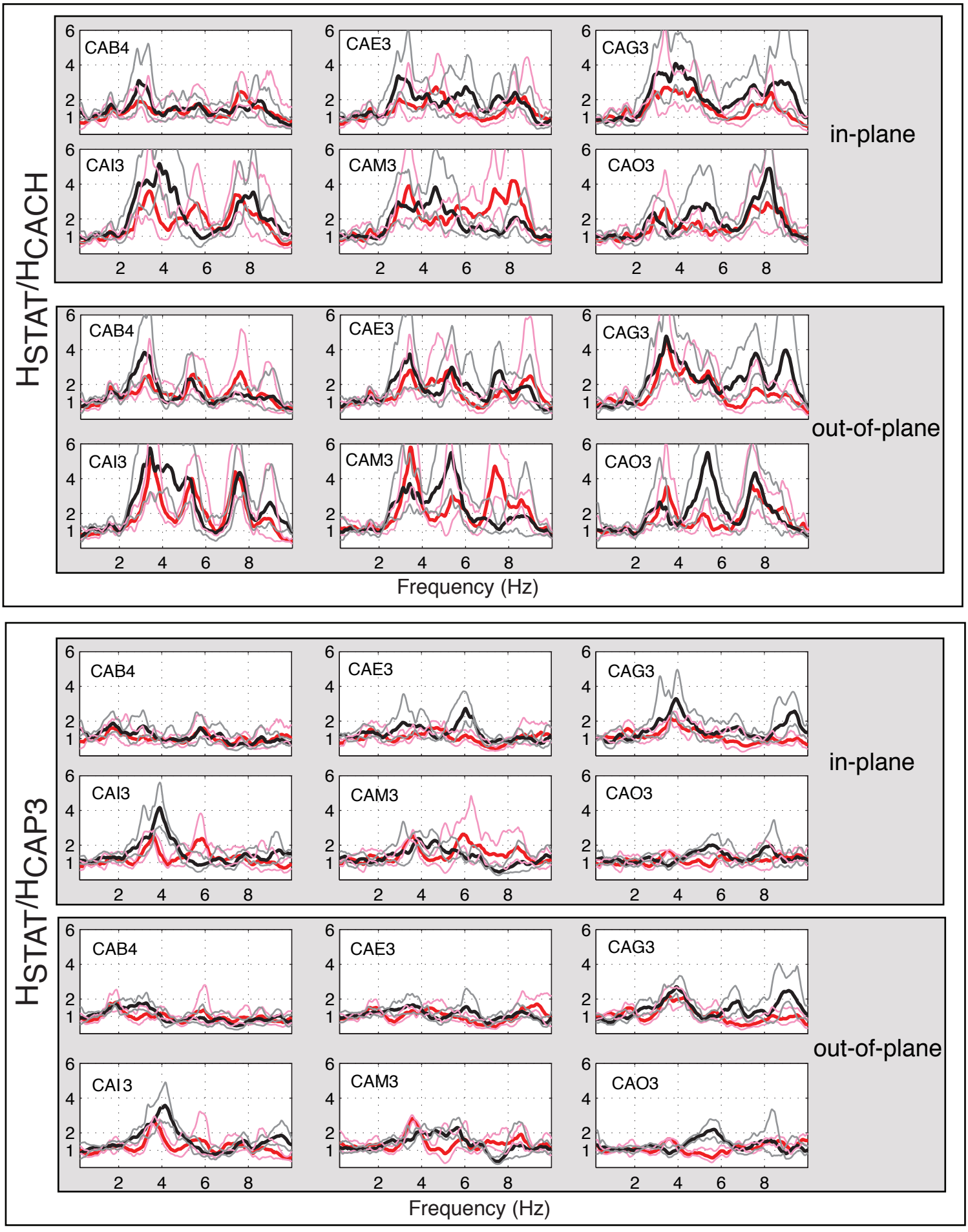
HSTAT/HCACH
HSTAT/HCAP3
CAB4
CAE3
CAG3
CAI3
CAM3
CAO3
in-plane
out-of-plane
Frequency (Hz)
East comp
North comp
East ± std
North ± std

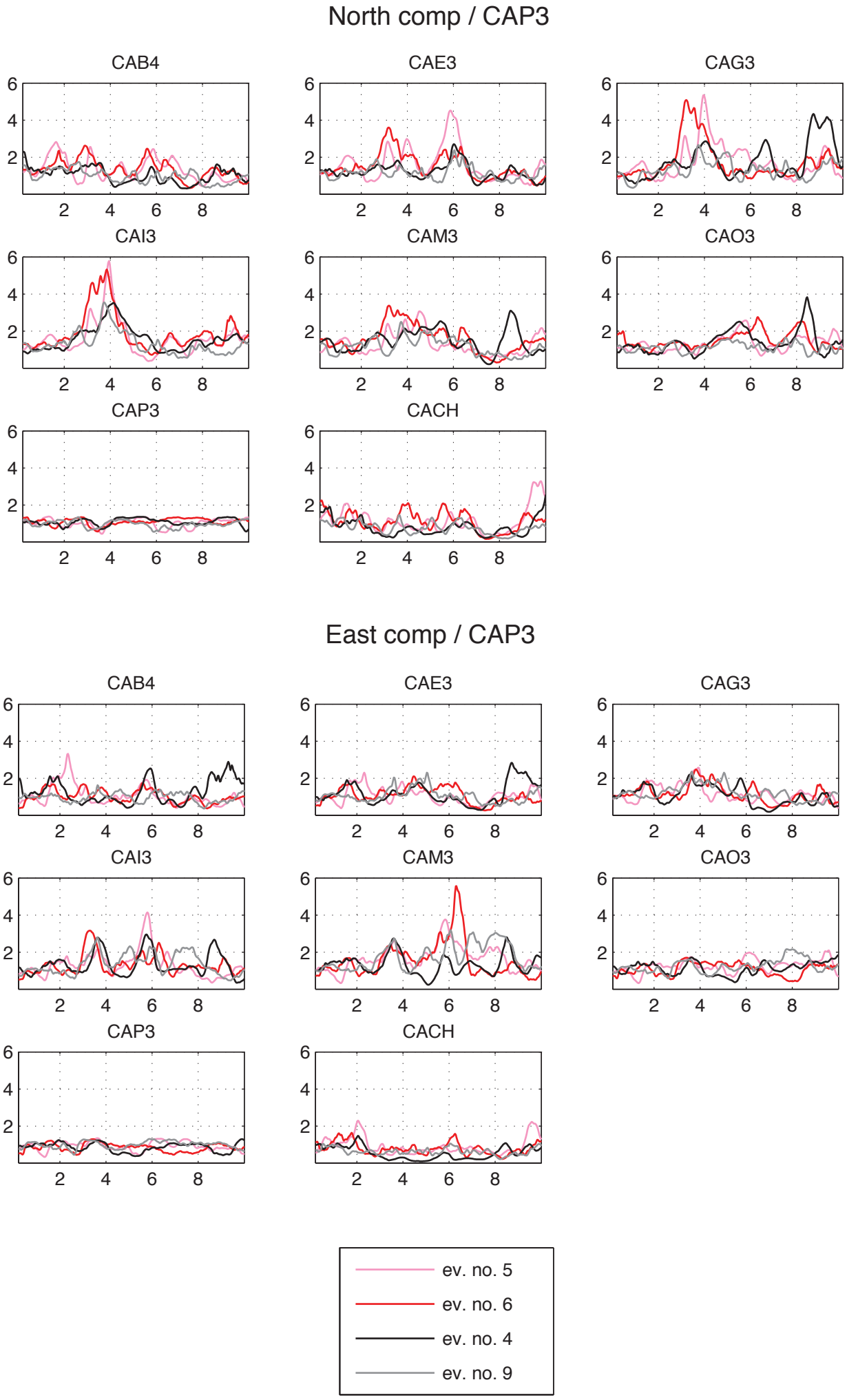
North comp / CAP3
CAB4
CAE3
CAG3
CAI3
CAM3
CAO3
CAP3
CACH
East comp / CAP3
CAB4
CAE3
CAG3
CAI3
CAM3
CAO3
CAP3
CACH
ev. no. 5
ev. no. 6
ev. no. 4
ev. no. 9

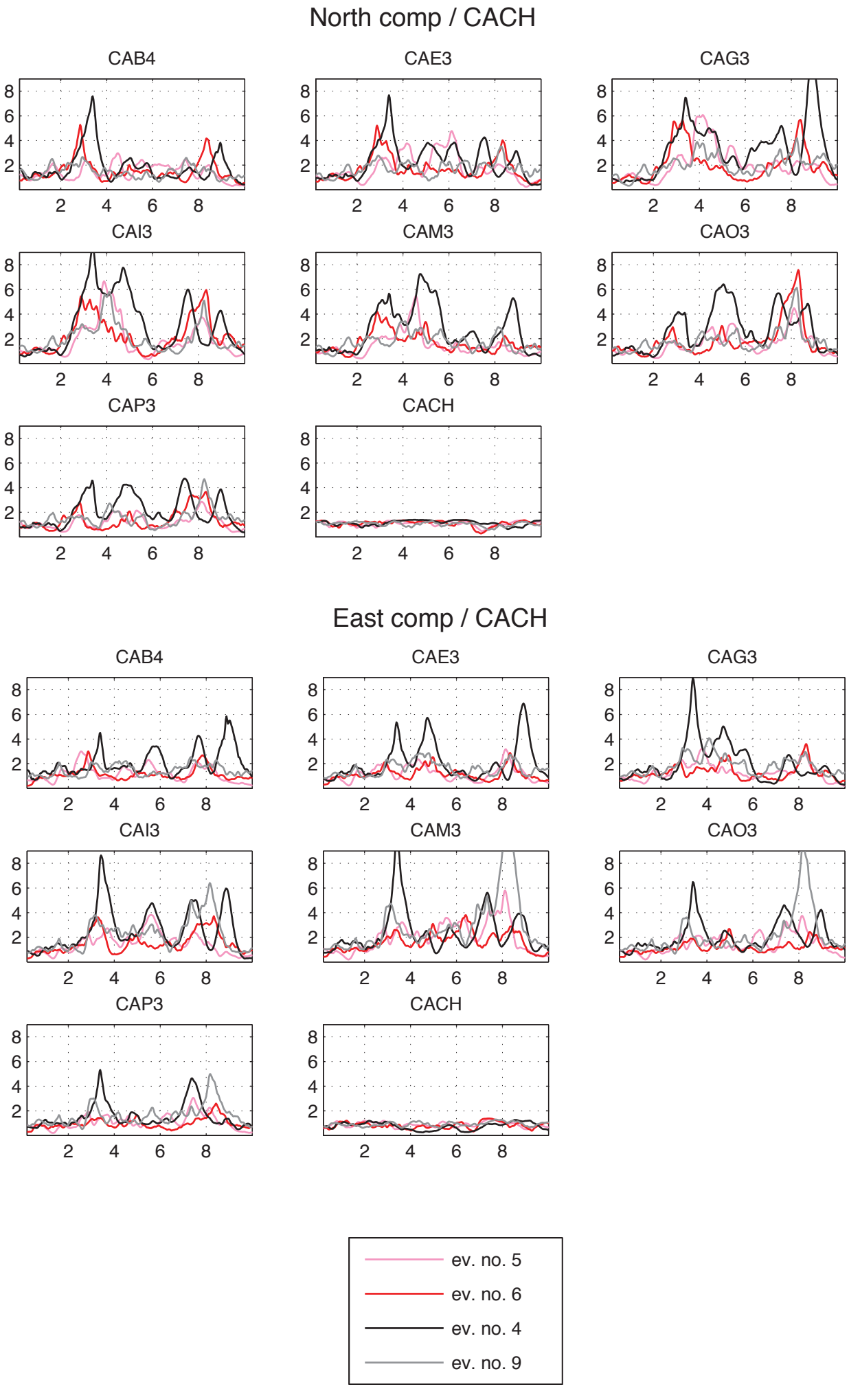
North comp / CACH
CAB4
CAE3
CAG3
CAI3
CAM3
CAO3
CAP3
CACH
East comp / CACH
CAB4
CAE3
CAG3
CAI3
CAM3
CAO3
CAP3
CACH
ev. no. 5
ev. no. 6
ev. no. 4
ev. no. 9

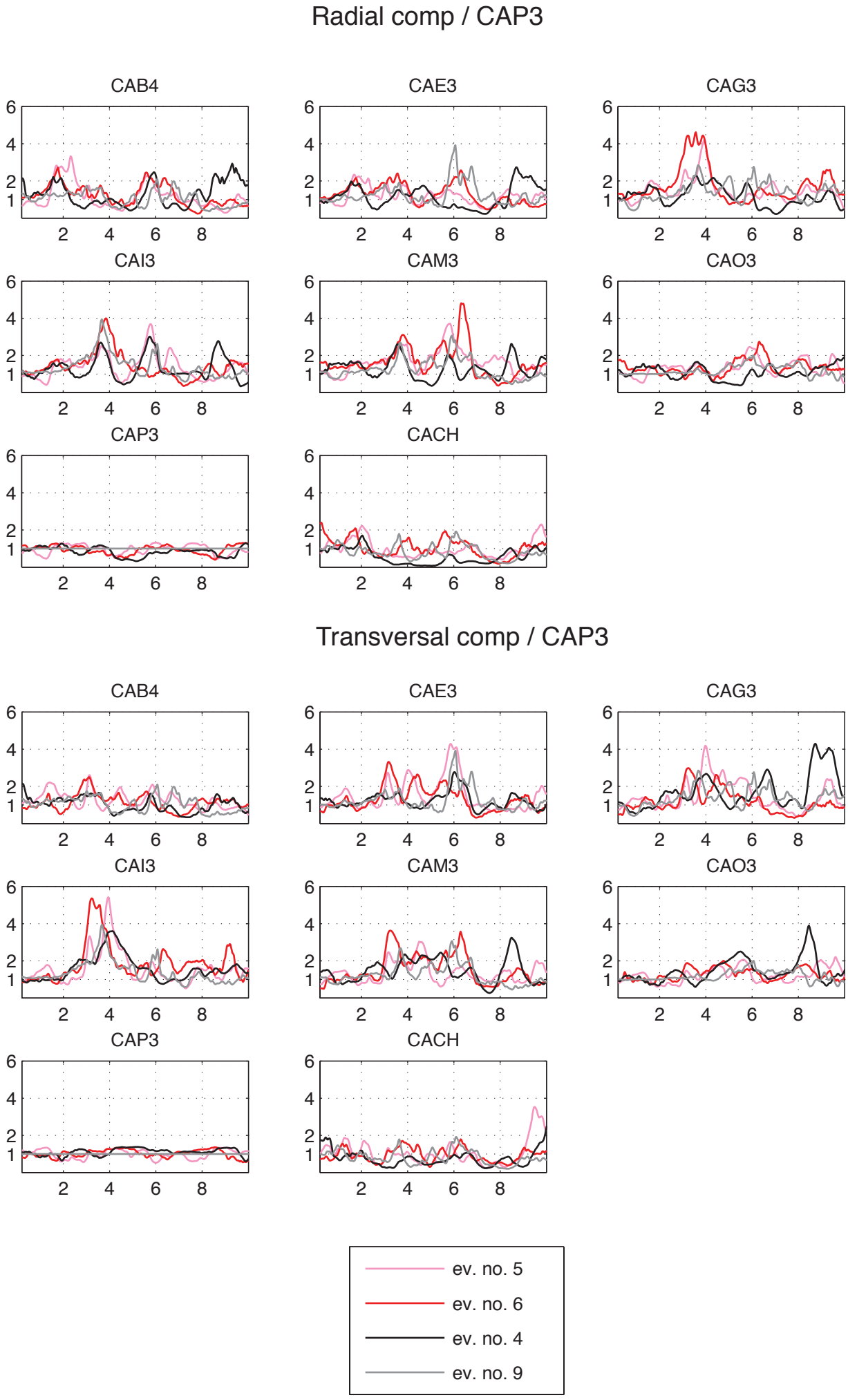
Radial comp / CAP3
CAB4
CAE3
CAG3
CAI3
CAM3
CAO3
CAP3
CACH
Transversal comp / CAP3
CAB4
CAE3
CAG3
CAI3
CAM3
CAO3
CAP3
CACH
ev. no. 5
ev. no. 6
ev. no. 4
ev. no. 9

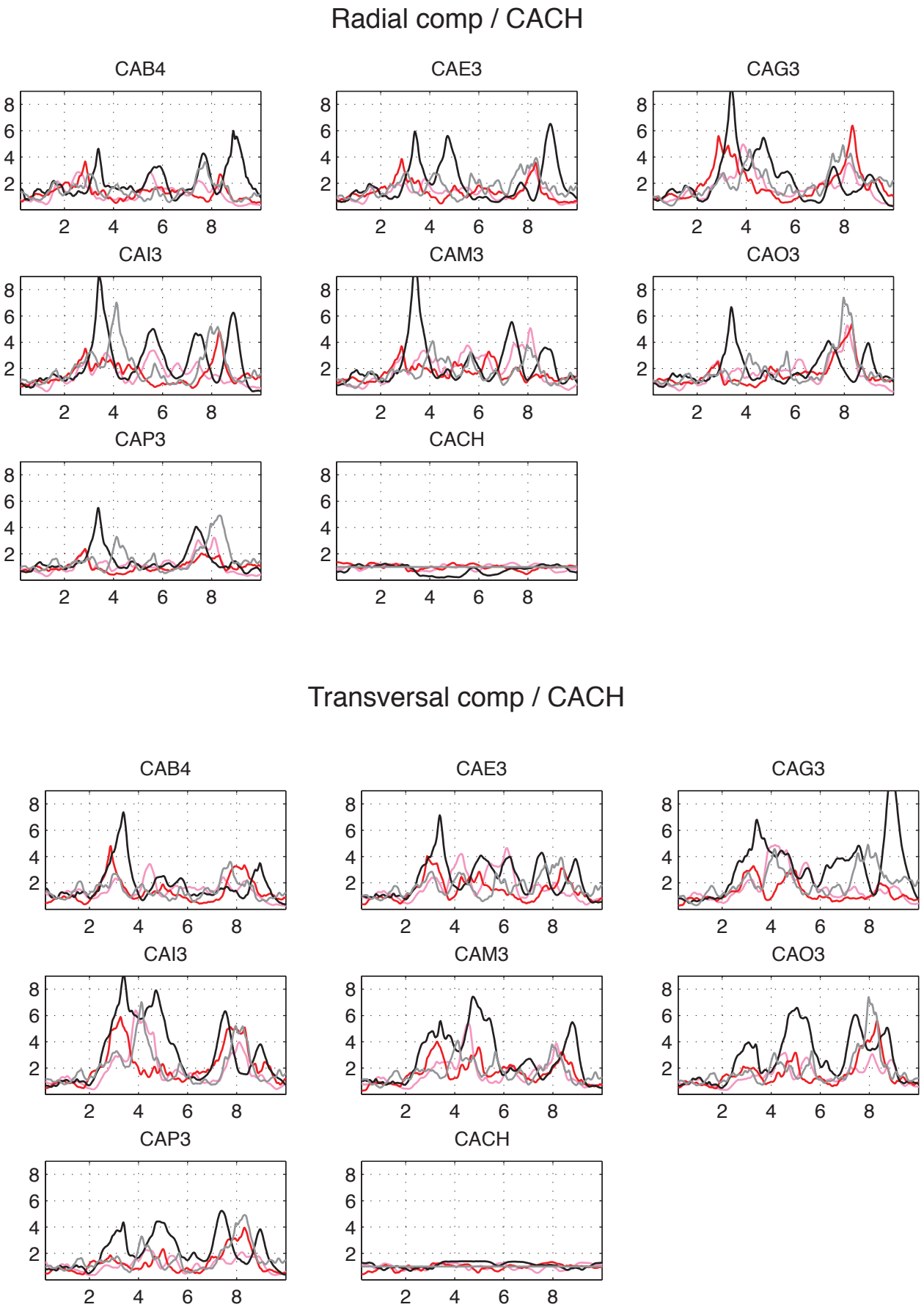
Radial comp / CACH
CAB4
CAE3
CAG3
CAI3
CAM3
CAO3
CAP3
CACH
Transversal comp / CACH
CAB4
CAE3
CAG3
CAI3
CAM3
CAO3
CAP3
CACH
ev. no. 5
ev. no. 6
ev. no. 4
ev. no. 9

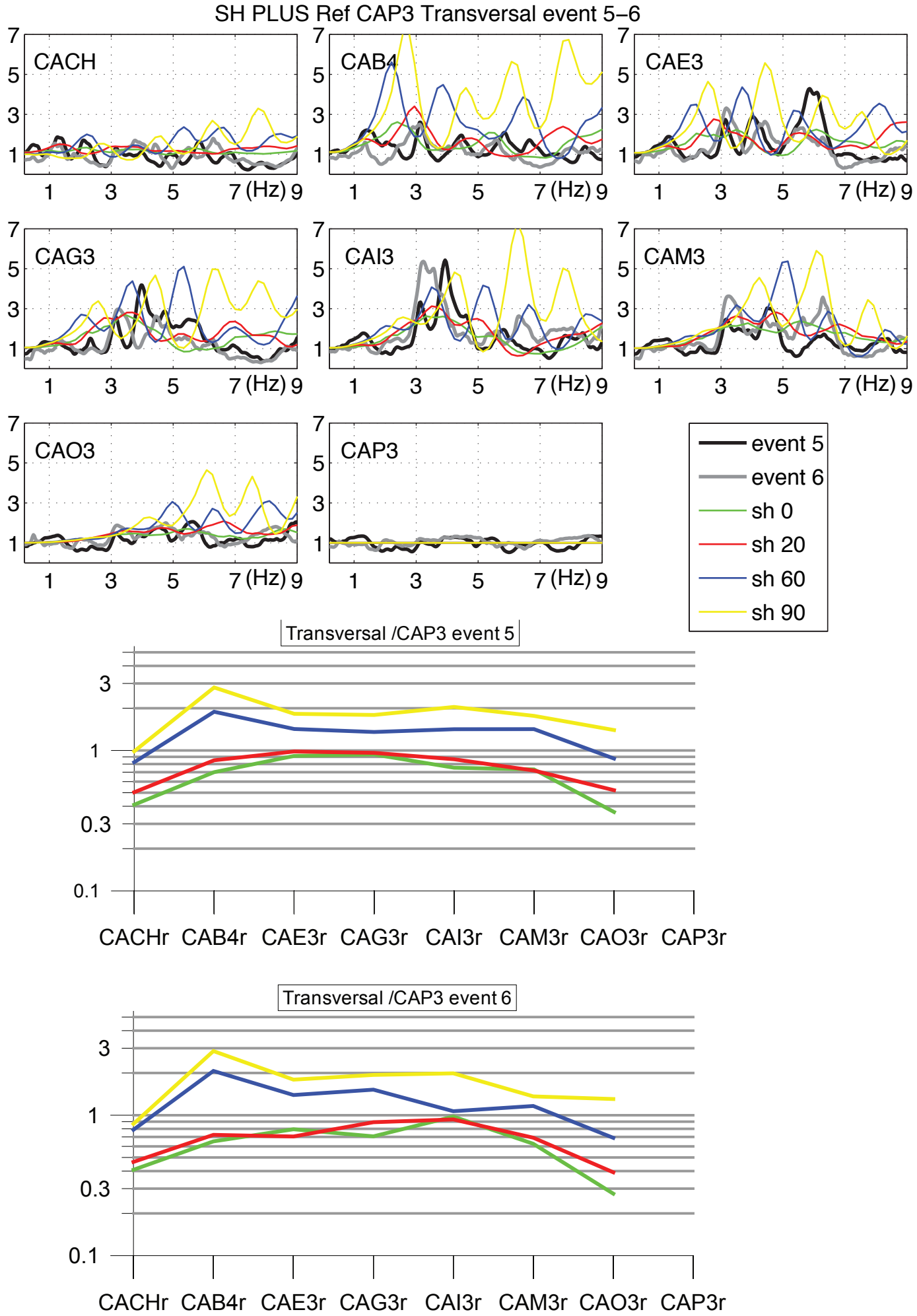
SH PLUS Ref CAP3 Transversal event 5–6
CACH
CAB4
CAE3
CAG3
CAI3
CAM3
CAO3
CAP3
7 (Hz) 9
event 5
event 6
sh 0
sh 20
sh 60
sh 90
Transversal /CAP3 event 5
Transversal /CAP3 event 6
CACHr CAB4r CAE3r CAG3r CAI3r CAM3r CAO3r CAP3r

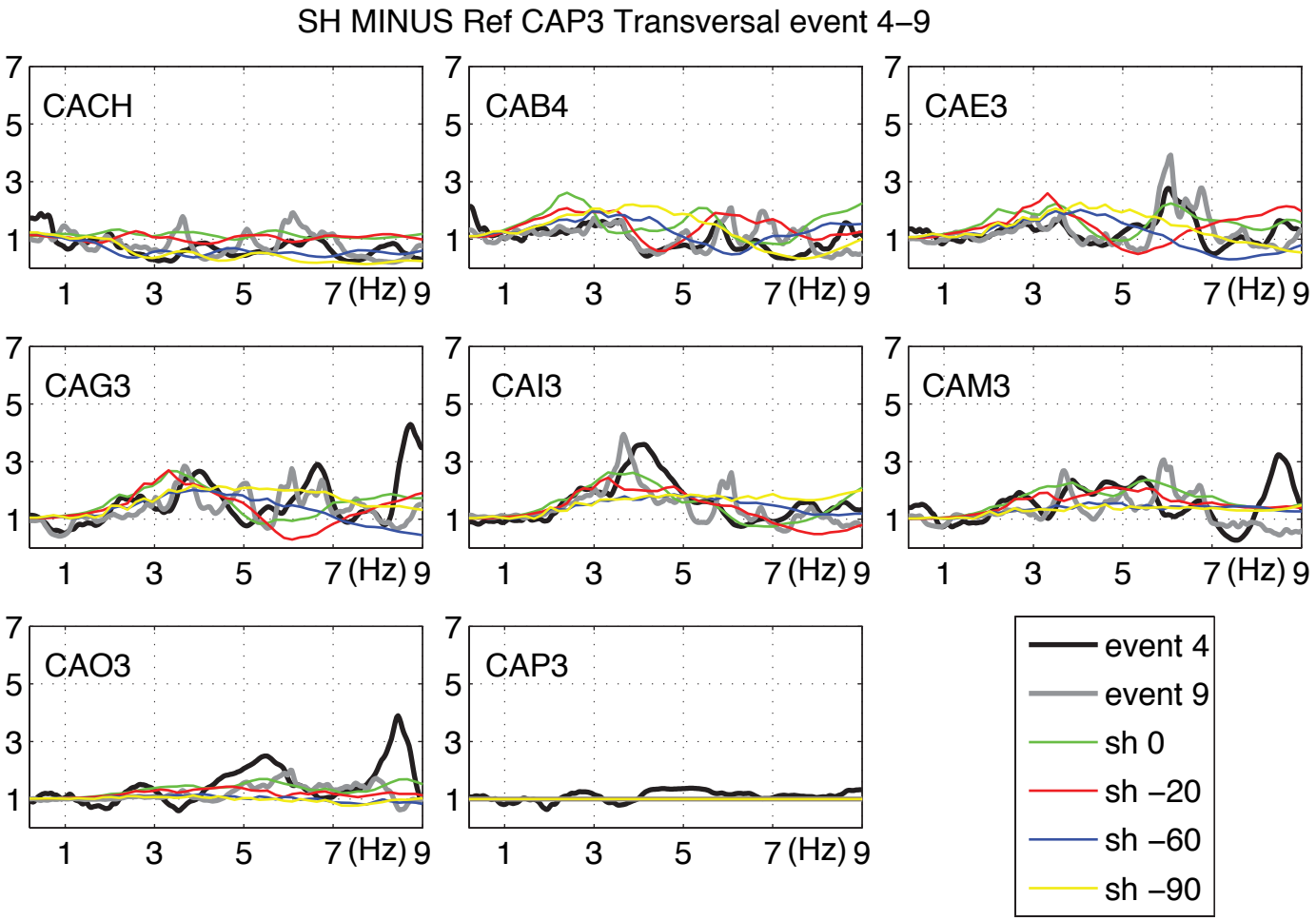
SH MINUS Ref CAP3 Transversal event 4–9
CACH
CAB4
CAE3
CAG3
CAI3
CAM3
CAO3
CAP3
7
5
3
1
1 3 5 7 (Hz) 9
event 4
event 9
sh 0
sh –20
sh –60
sh –90

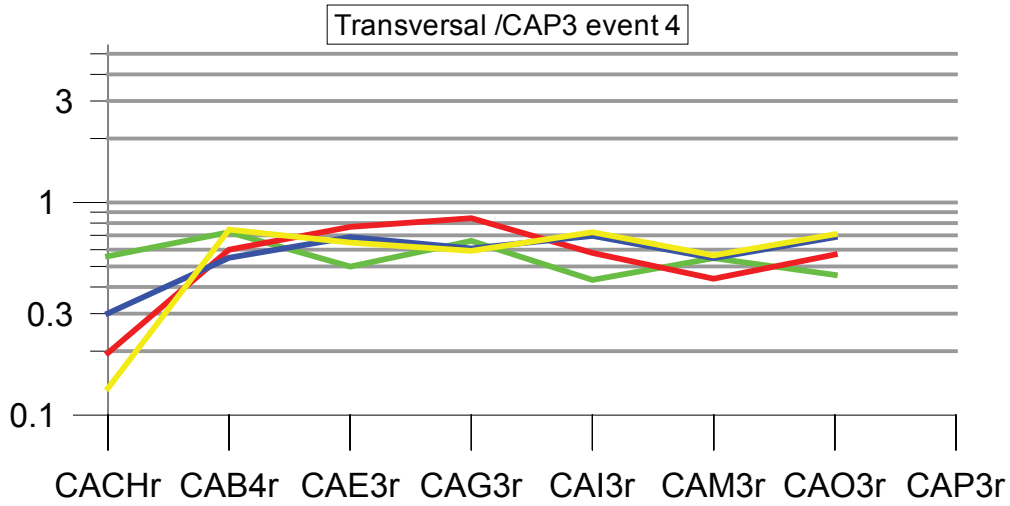
Transversal /CAP3 event 4
3
1
0.3
0.1
CACHr CAB4r CAE3r CAG3r CAI3r CAM3r CAO3r CAP3r

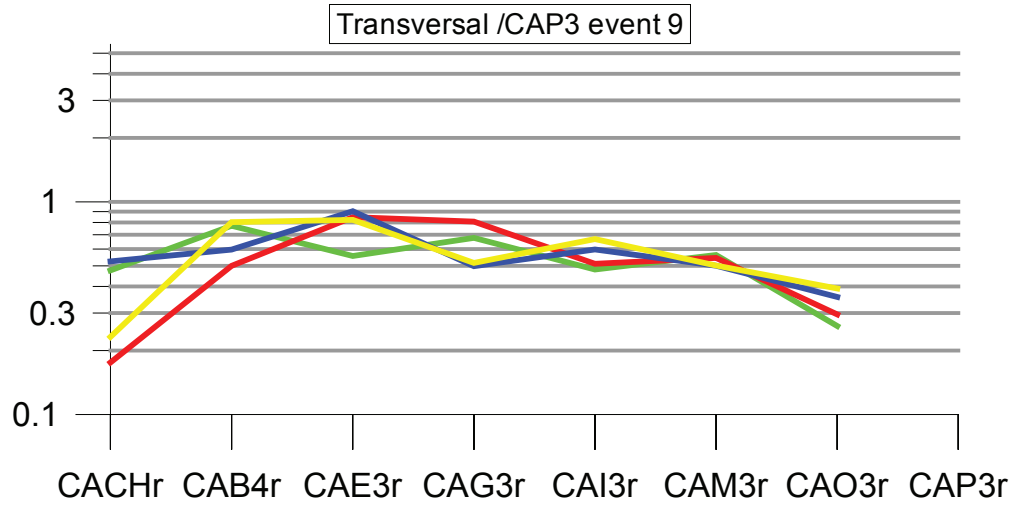
Transversal /CAP3 event 9
3
1
0.3
0.1
CACHr CAB4r CAE3r CAG3r CAI3r CAM3r CAO3r CAP3r

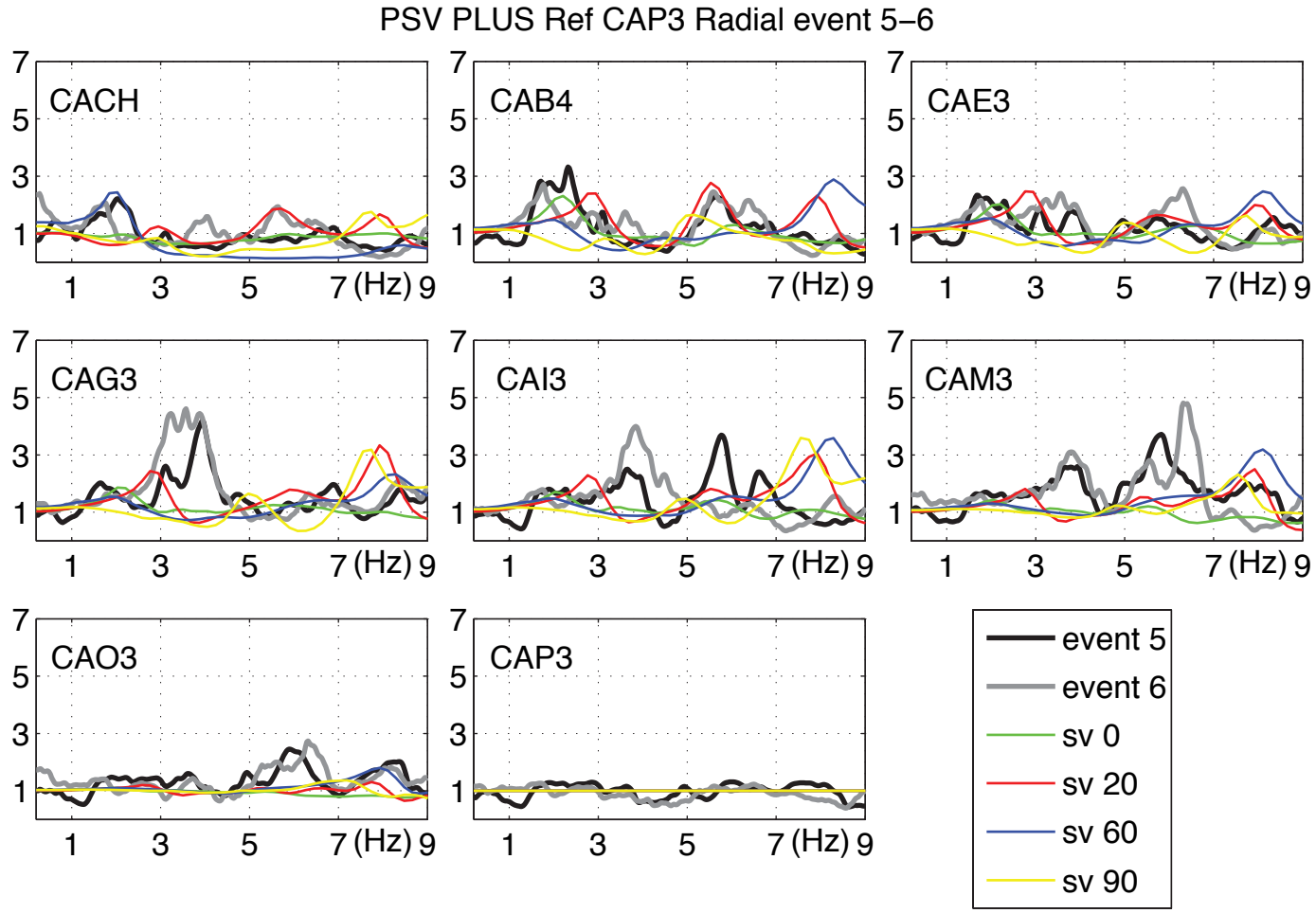
PSV PLUS Ref CAP3 Radial event 5–6
CACH
CAB4
CAE3
CAG3
CAI3
CAM3
CAO3
CAP3
7
5
3
1
1 3 5 7 (Hz) 9
event 5
event 6
sv 0
sv 20
sv 60
sv 90

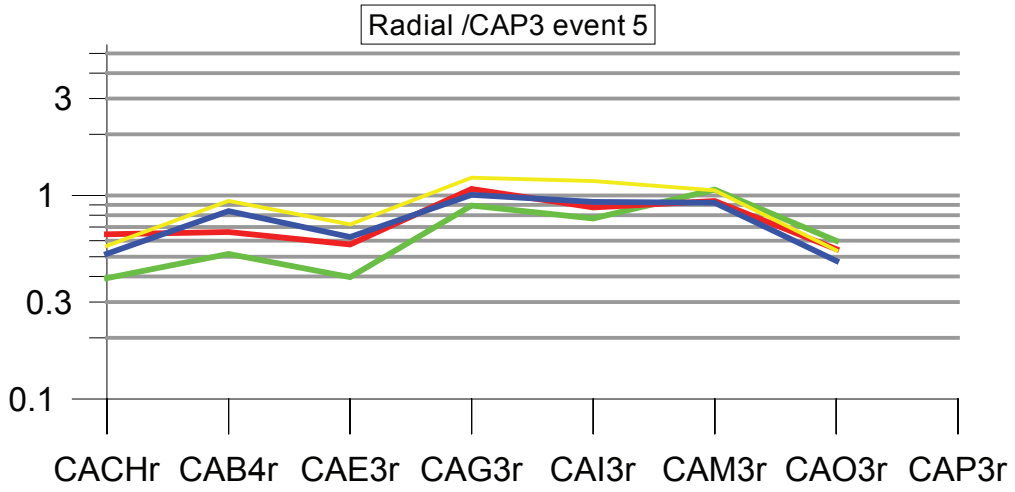
Radial /CAP3 event 5
3
1
0.3
0.1
CACHr CAB4r CAE3r CAG3r CAI3r CAM3r CAO3r CAP3r

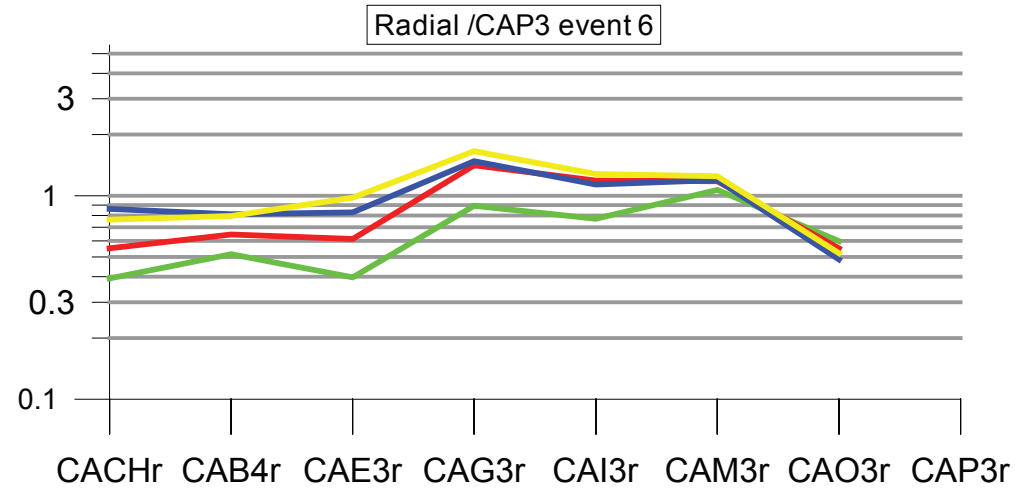
Radial /CAP3 event 6
3
1
0.3
0.1
CACHr CAB4r CAE3r CAG3r CAI3r CAM3r CAO3r CAP3r

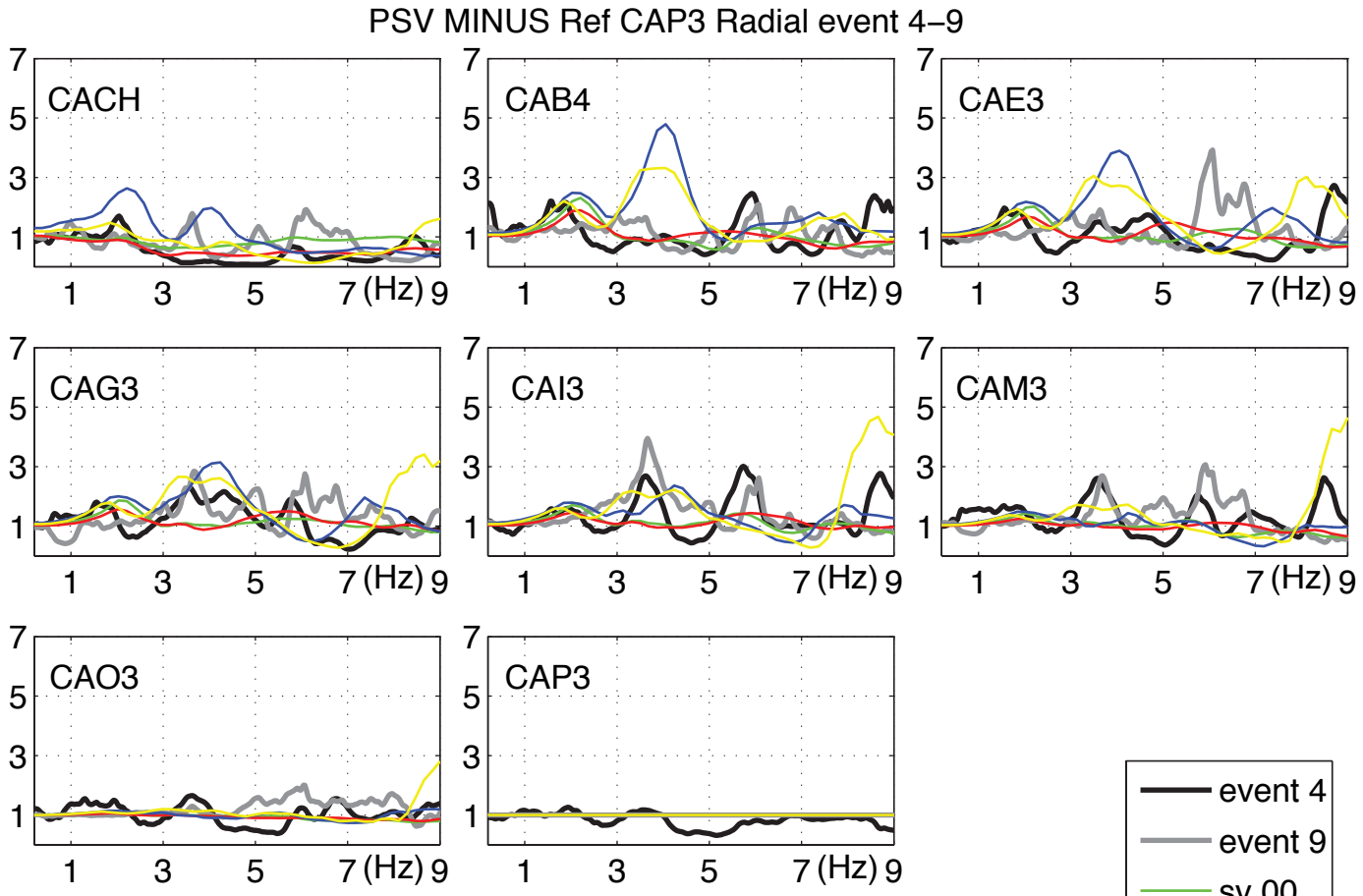
PSV MINUS Ref CAP3 Radial event 4–9
CACH
CAB4
CAE3
CAG3
CAI3
CAM3
CAO3
CAP3
7
5
3
1
1 3 5 7 (Hz) 9
event 4
event 9
sv 00
sv –20
sv –60
sv –90

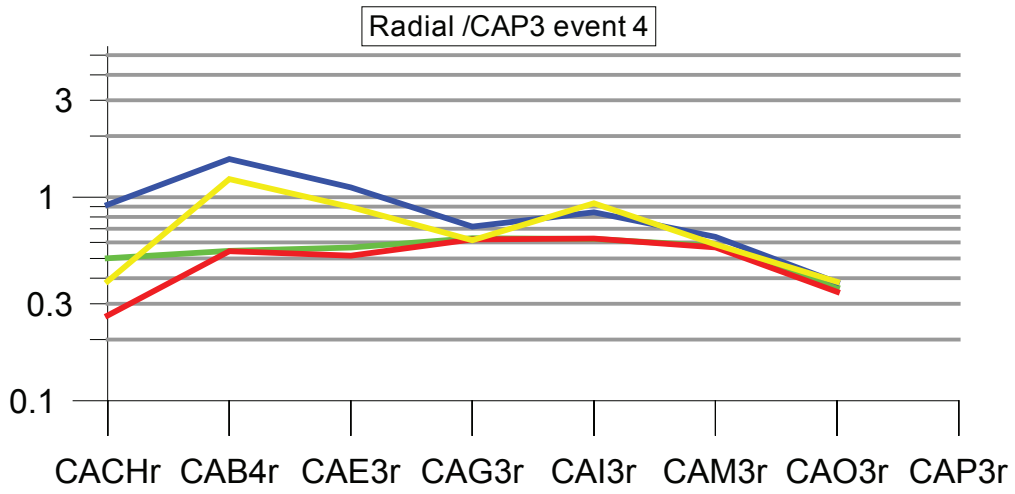
Radial /CAP3 event 4
3
1
0.3
0.1
CACHr CAB4r CAE3r CAG3r CAI3r CAM3r CAO3r CAP3r

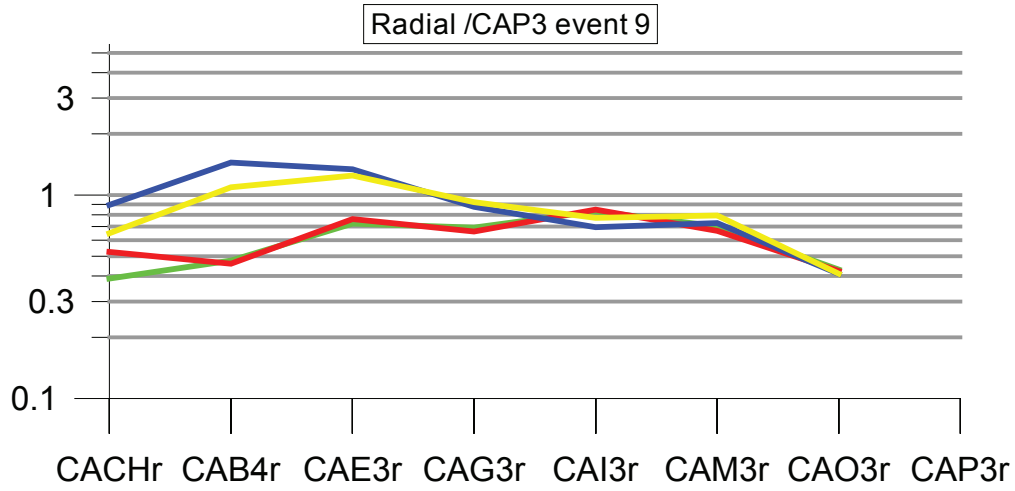
Radial /CAP3 event 9
3
1
0.3
0.1
CACHr CAB4r CAE3r CAG3r CAI3r CAM3r CAO3r CAP3r

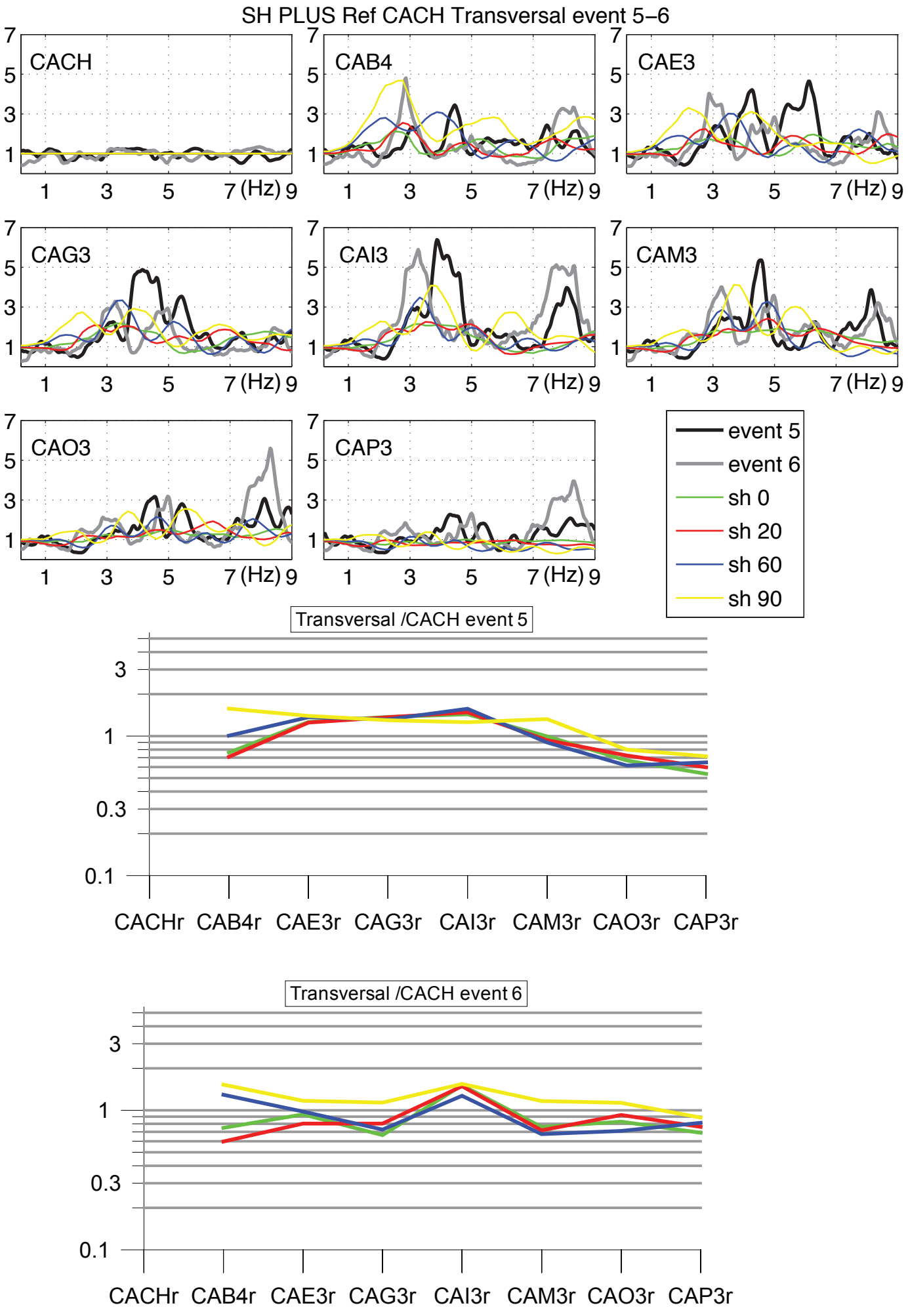
SH PLUS Ref CACH Transversal event 5–6
CACH
CAB4
CAE3
CAG3
CAI3
CAM3
CAO3
CAP3
7
5
3
1
1 3 5 7 (Hz) 9
event 5
event 6
sh 0
sh 20
sh 60
sh 90
Transversal /CACH event 5
3
1
0.3
0.1
CACHr CAB4r CAE3r CAG3r CAI3r CAM3r CAO3r CAP3r
Transversal /CACH event 6
3
1
0.3
0.1
CACHr CAB4r CAE3r CAG3r CAI3r CAM3r CAO3r CAP3r

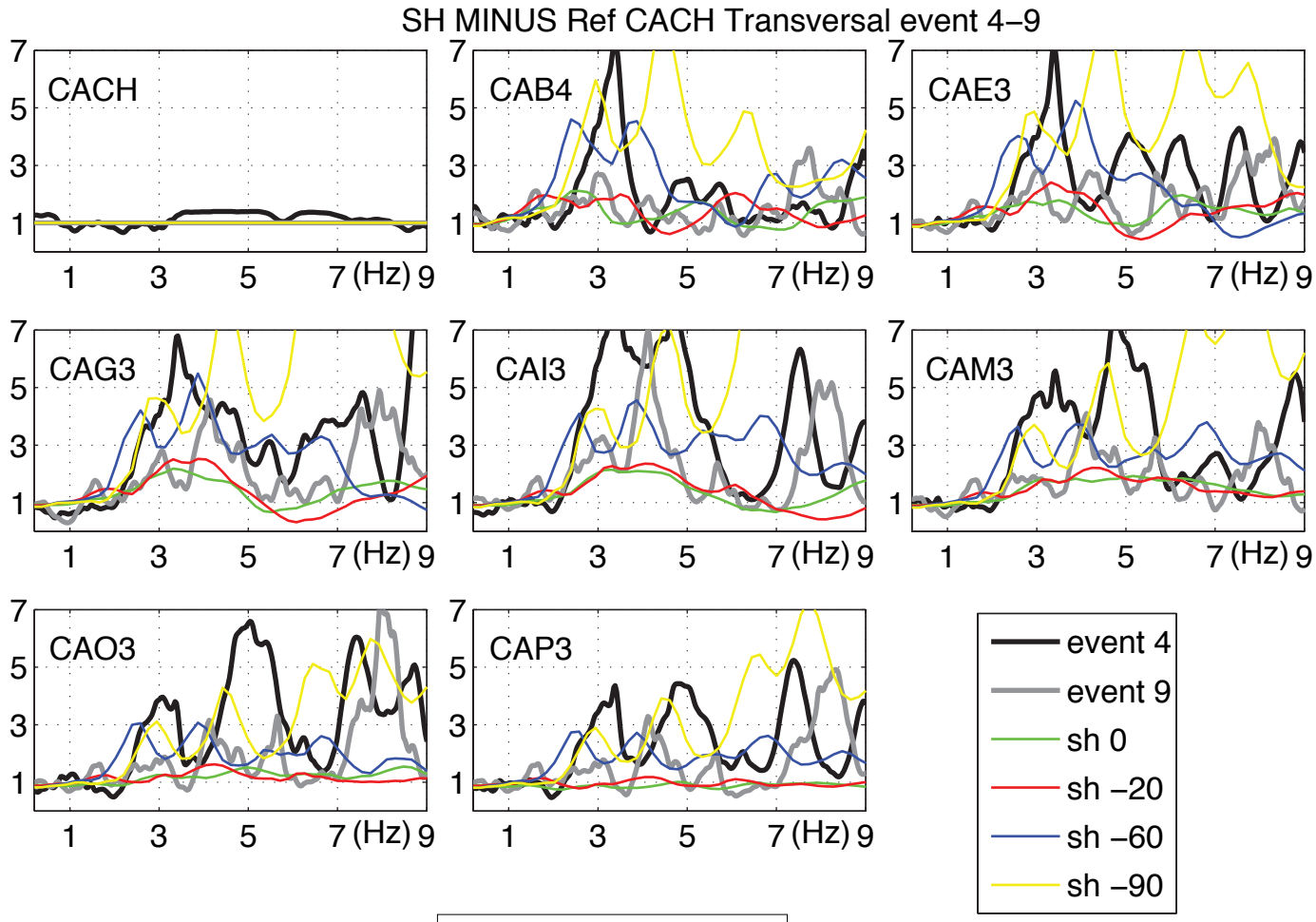
SH MINUS Ref CACH Transversal event 4–9
CACH
CAB4
CAE3
CAG3
CAI3
CAM3
CAO3
CAP3
7
5
3
1
1
3
5
7 (Hz) 9
event 4
event 9
sh 0
sh –20
sh –60
sh –90

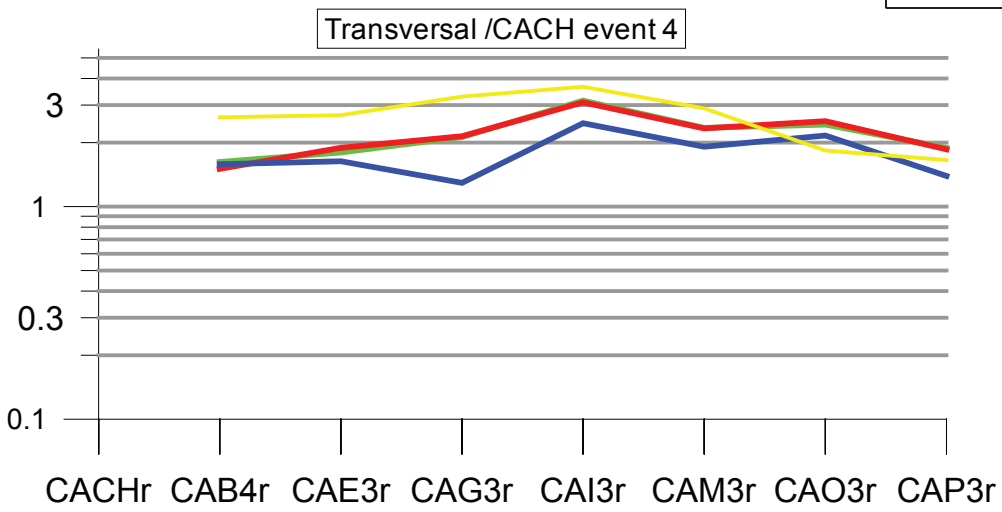
Transversal /CACH event 4
3
1
0.3
0.1
CACHr
CAB4r
CAE3r
CAG3r
CAI3r
CAM3r
CAO3r
CAP3r

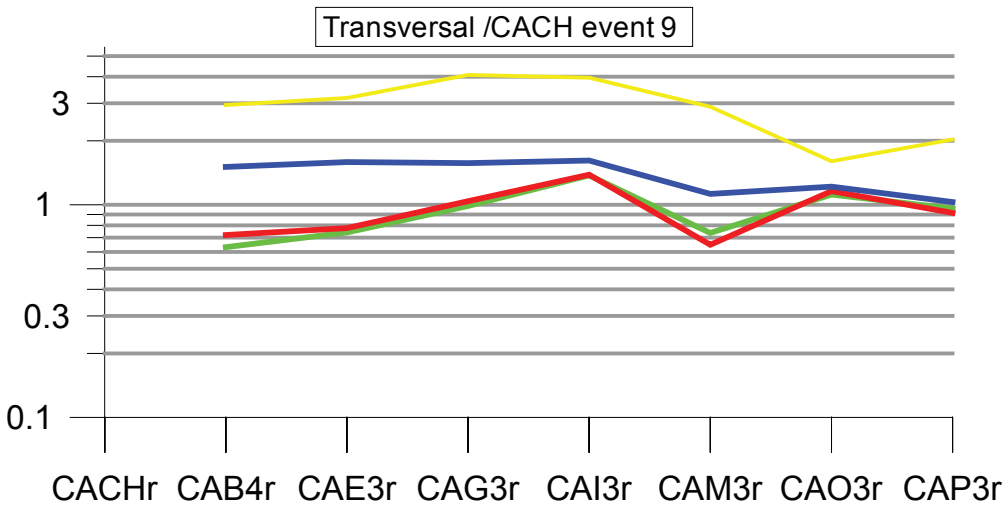
Transversal /CACH event 9
3
1
0.3
0.1
CACHr
CAB4r
CAE3r
CAG3r
CAI3r
CAM3r
CAO3r
CAP3r

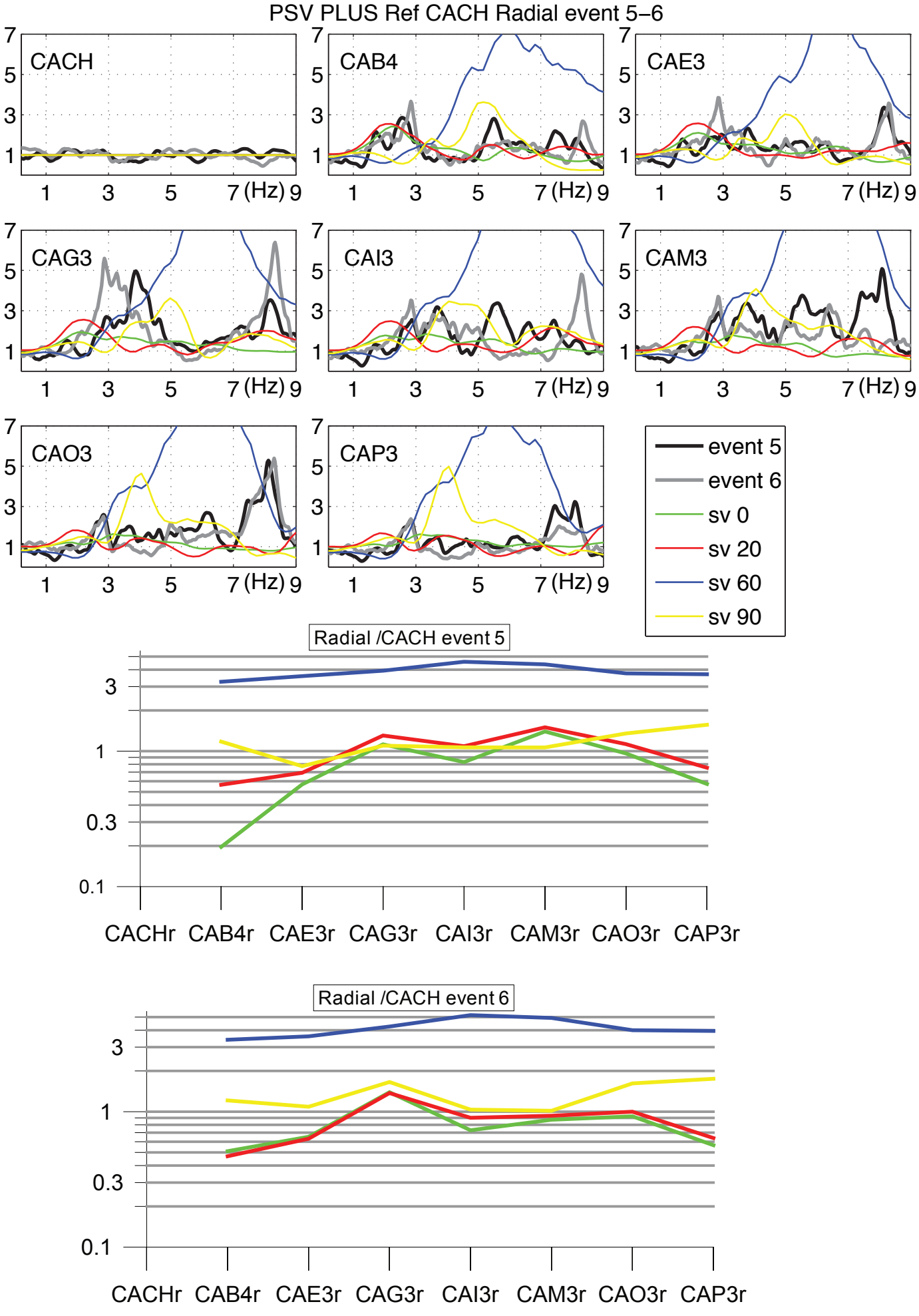
PSV PLUS Ref CACH Radial event 5–6
CACH
CAB4
CAE3
CAG3
CAI3
CAM3
CAO3
CAP3
7 (Hz) 9
event 5
event 6
sv 0
sv 20
sv 60
sv 90
Radial /CACH event 5
Radial /CACH event 6
CACHr CAB4r CAE3r CAG3r CAI3r CAM3r CAO3r CAP3r

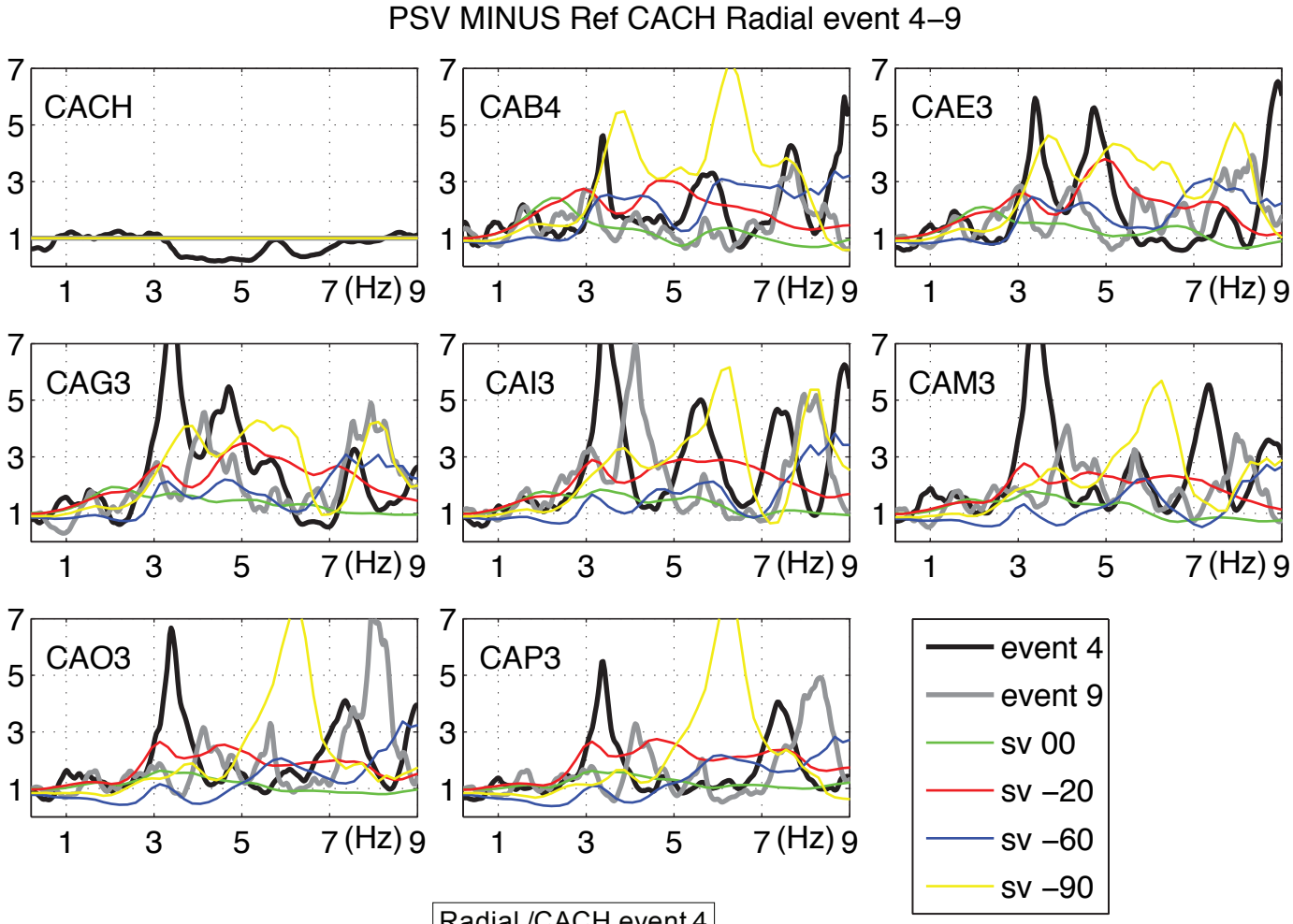
PSV MINUS Ref CACH Radial event 4–9
CACH
CAB4
CAE3
CAG3
CAI3
CAM3
CAO3
CAP3
7
5
3
1
1 3 5 7 (Hz) 9
event 4
event 9
sv 00
sv –20
sv –60
sv –90

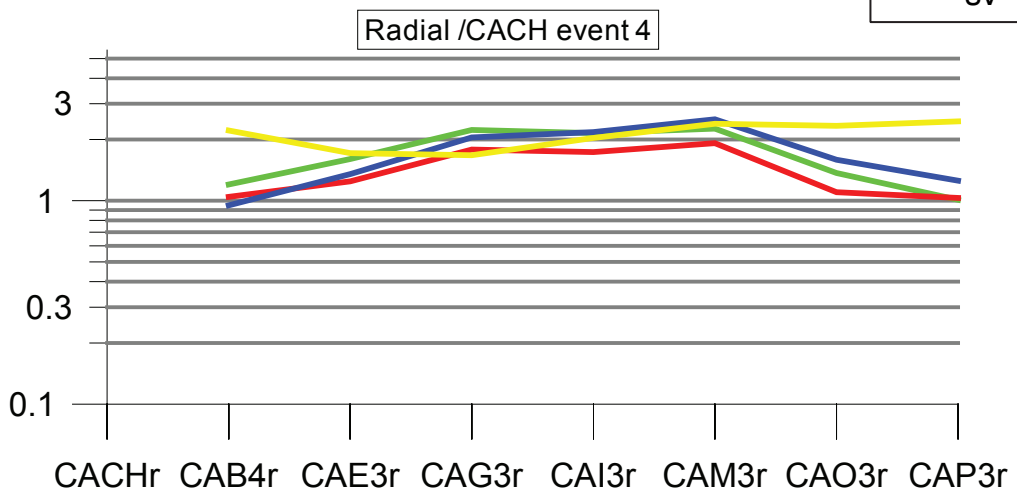
Radial /CACH event 4
3
1
0.3
0.1
CACHr CAB4r CAE3r CAG3r CAI3r CAM3r CAO3r CAP3r

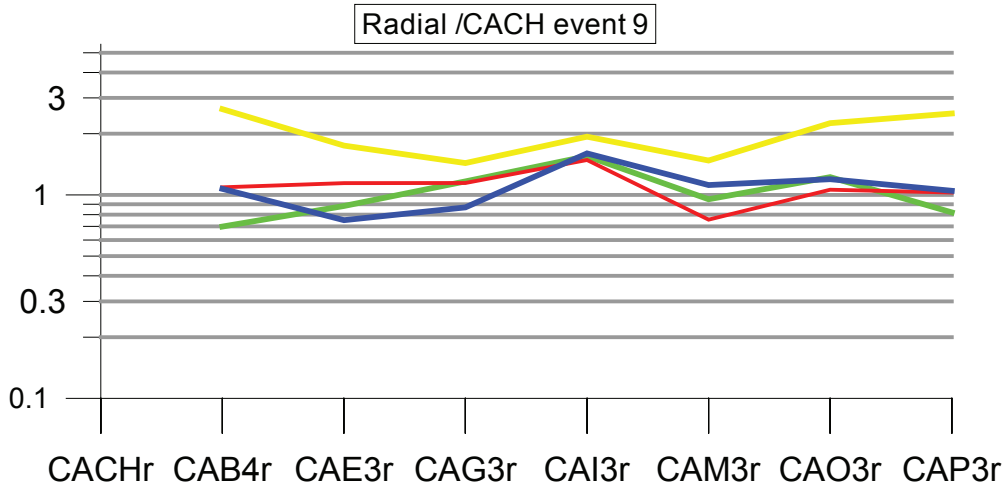
Radial /CACH event 9
3
1
0.3
0.1
CACHr CAB4r CAE3r CAG3r CAI3r CAM3r CAO3r CAP3r

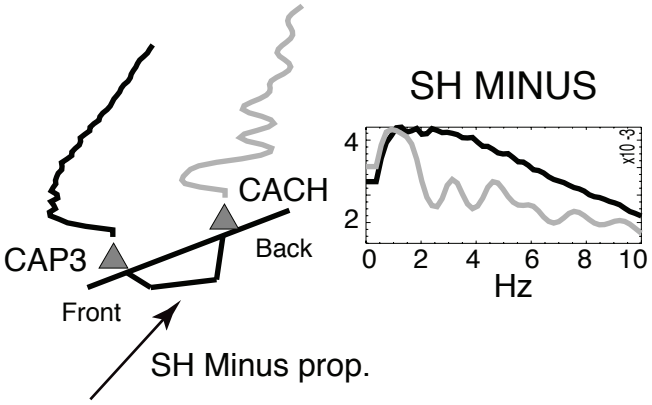
SH MINUS
CACH
CAP3
Back
Front
SH Minus prop.
x10-3
Hz

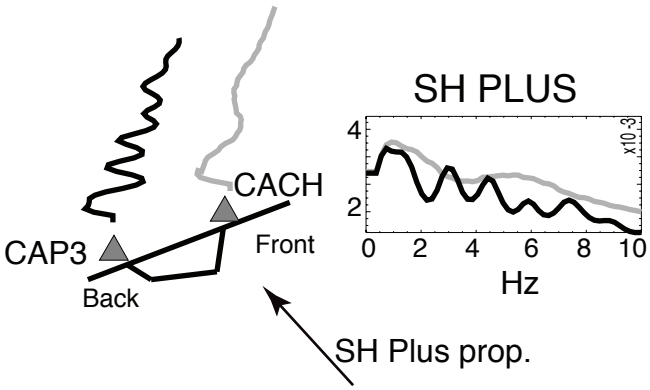
SH PLUS
CACH
CAP3
Front
Back
SH Plus prop.
x10-3
Hz

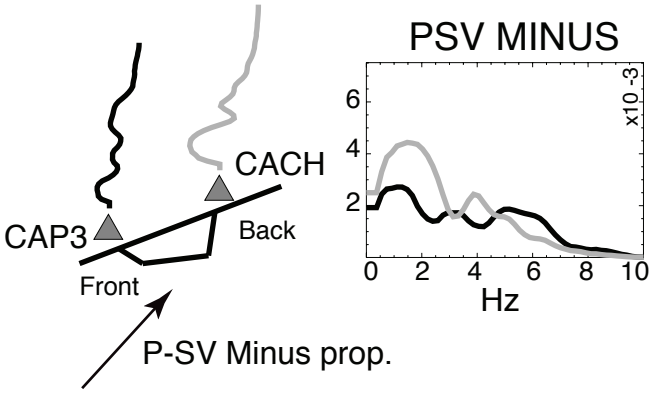
PSV MINUS
CACH
CAP3
Back
Front
P-SV Minus prop.
x10 -3
Hz

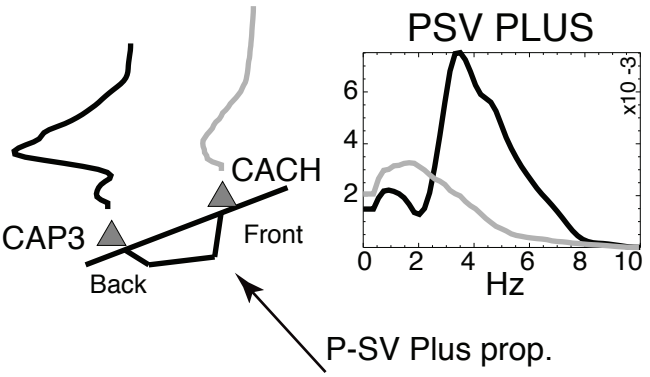
PSV PLUS
CACH
CAP3
Front
Back
P-SV Plus prop.
x10 -3
Hz

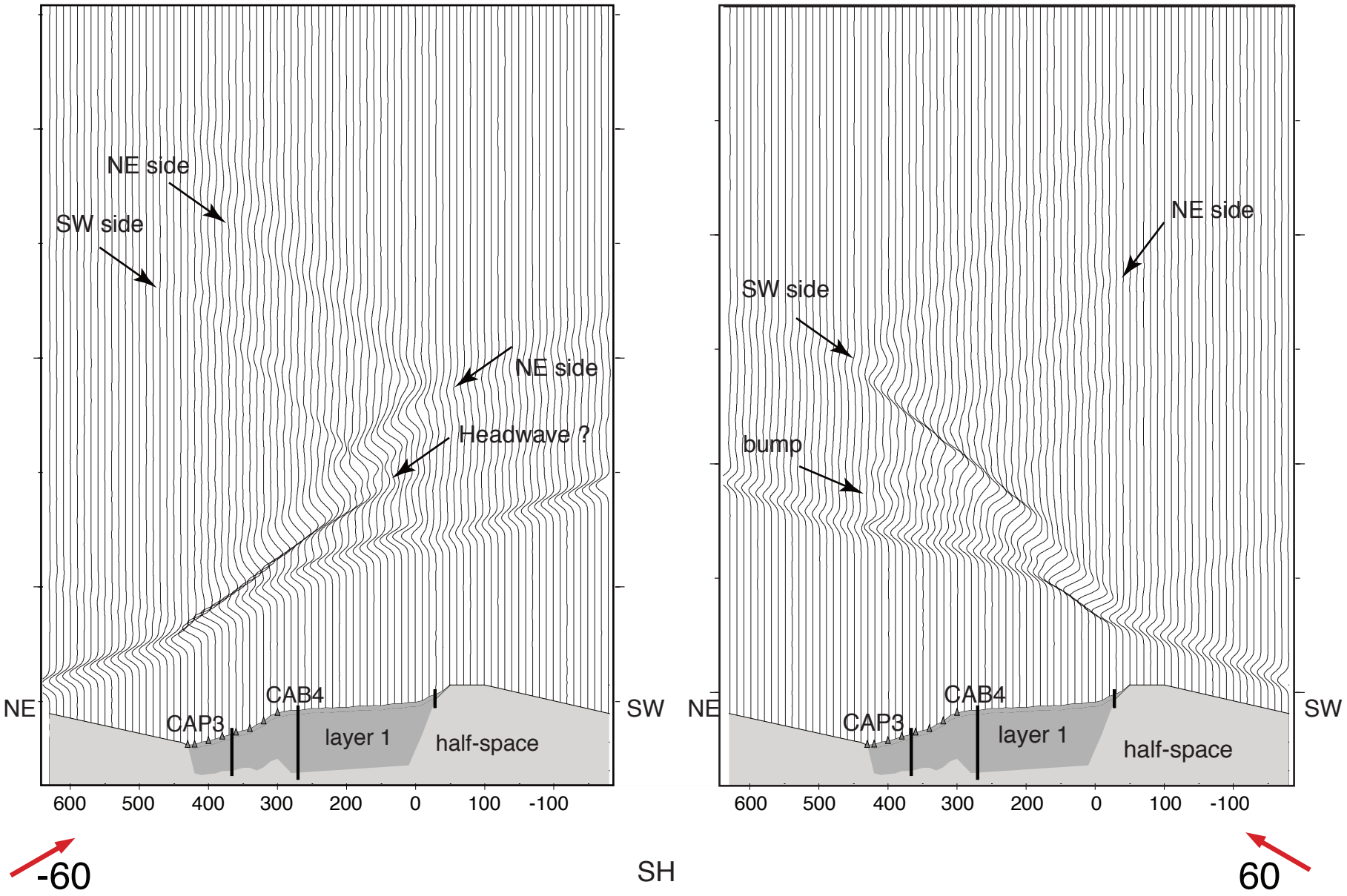
NE side
SW side
NE side
Headwave ?
NE
SW
CAP3
CAB4
layer 1
half-space
600
500
400
300
200
0
100
-100
-60
SH
SW side
NE side
bump
NE
SW
CAP3
CAB4
layer 1
half-space
600
500
400
300
200
0
100
-100
60

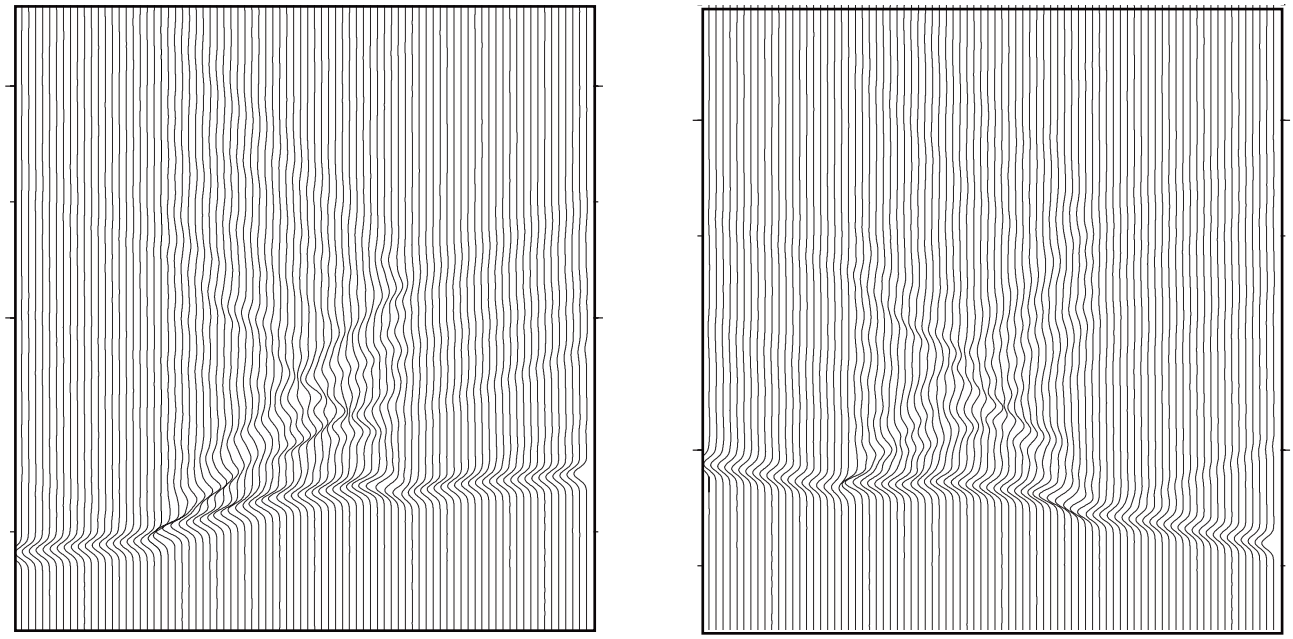

SH

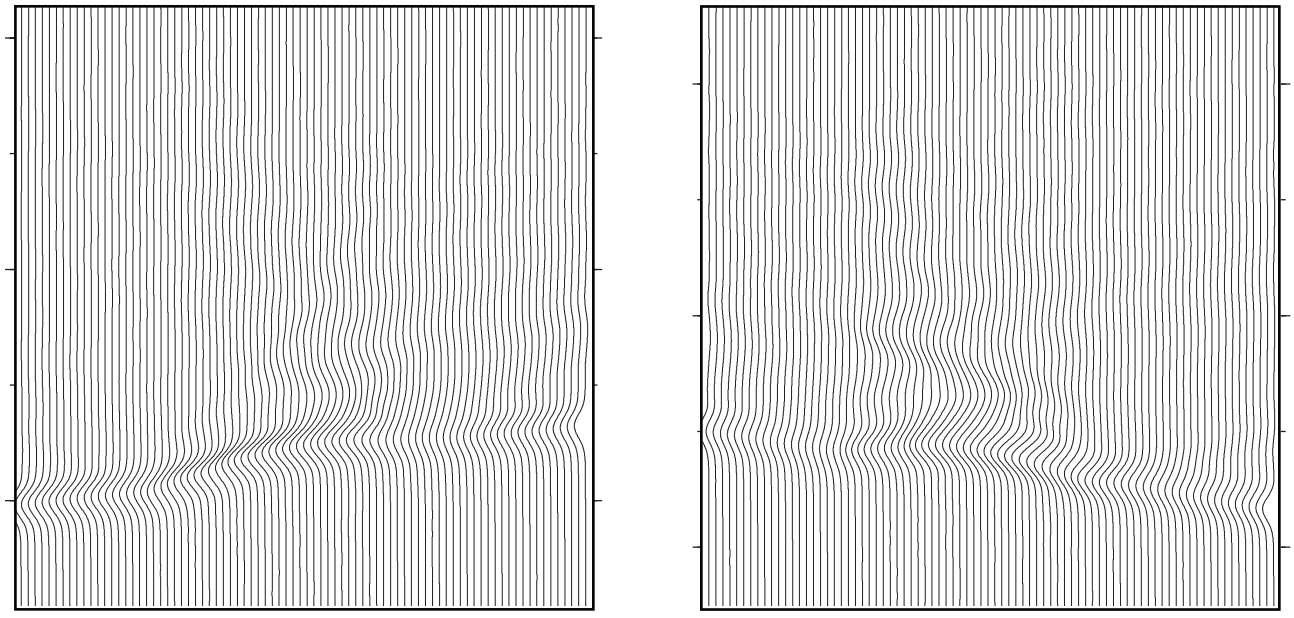

PSV U_X

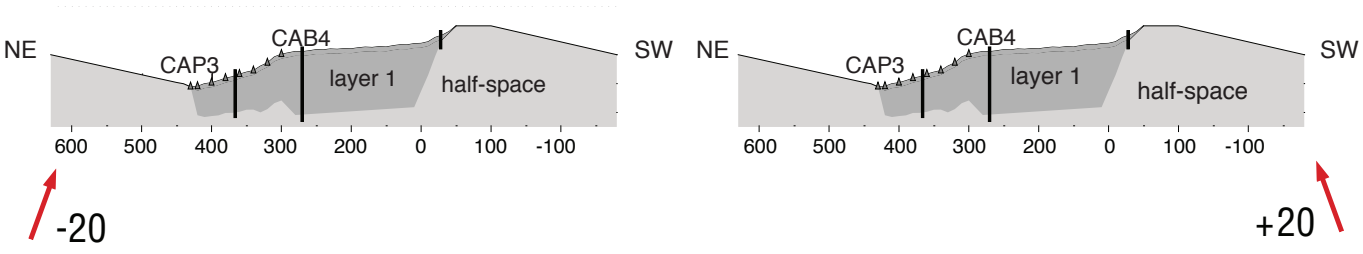

-20

+20

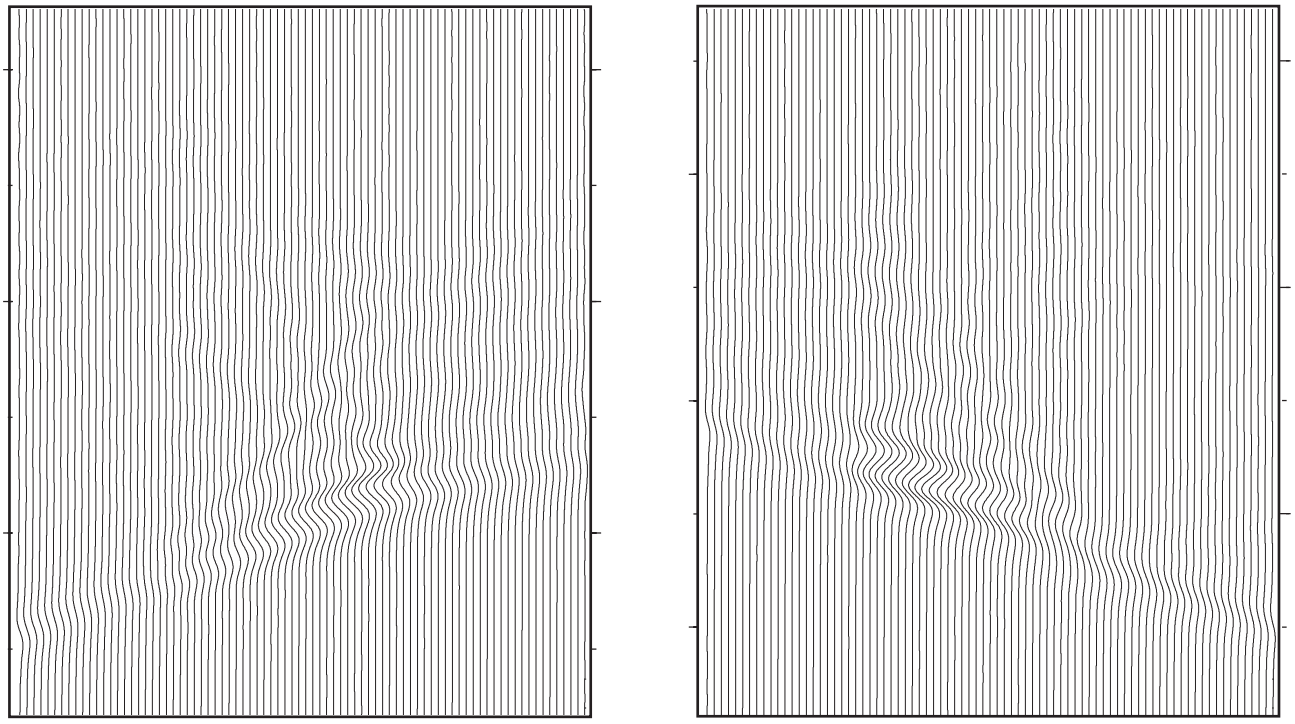

PSV Ux

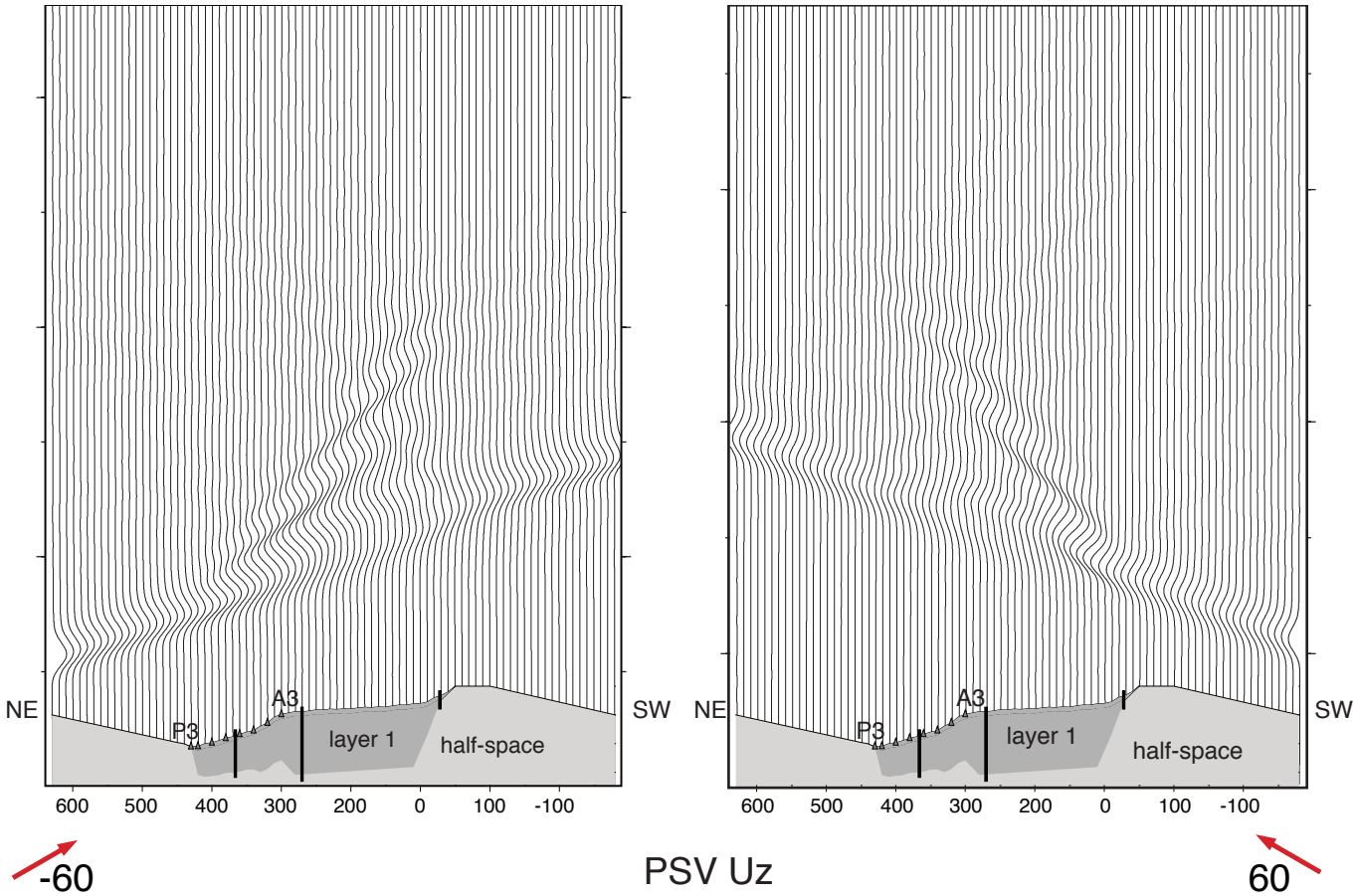

-60

PSV Uz

60

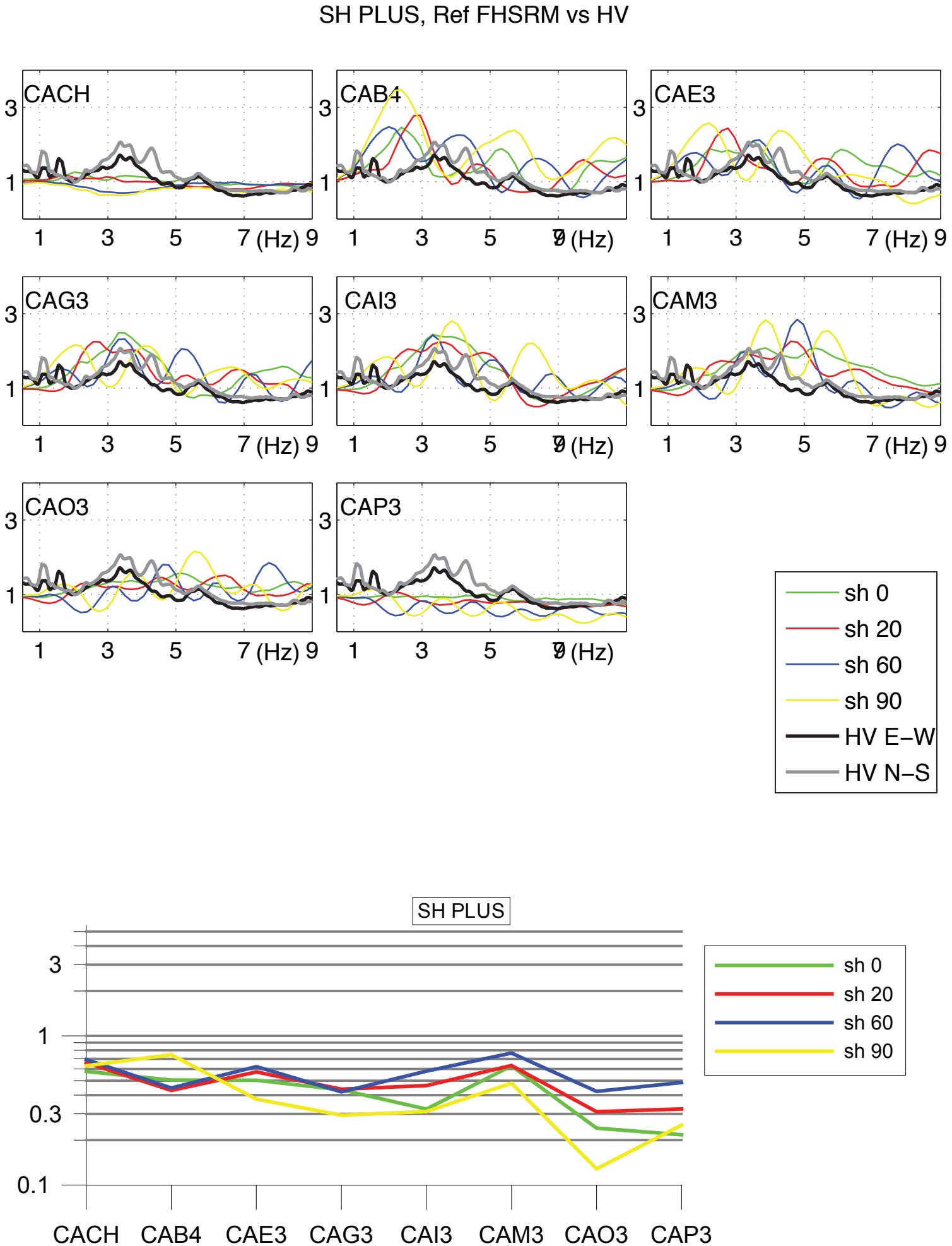
SH PLUS, Ref FHSRM vs HV
CACH
CAB4
CAE3
CAG3
CAI3
CAM3
CAO3
CAP3
3
1
1 3 5 7 (Hz) 9
sh 0
sh 20
sh 60
sh 90
HV E–W
HV N–S
SH PLUS
3
1
0.3
0.1
CACH CAB4 CAE3 CAG3 CAI3 CAM3 CAO3 CAP3
sh 0
sh 20
sh 60
sh 90

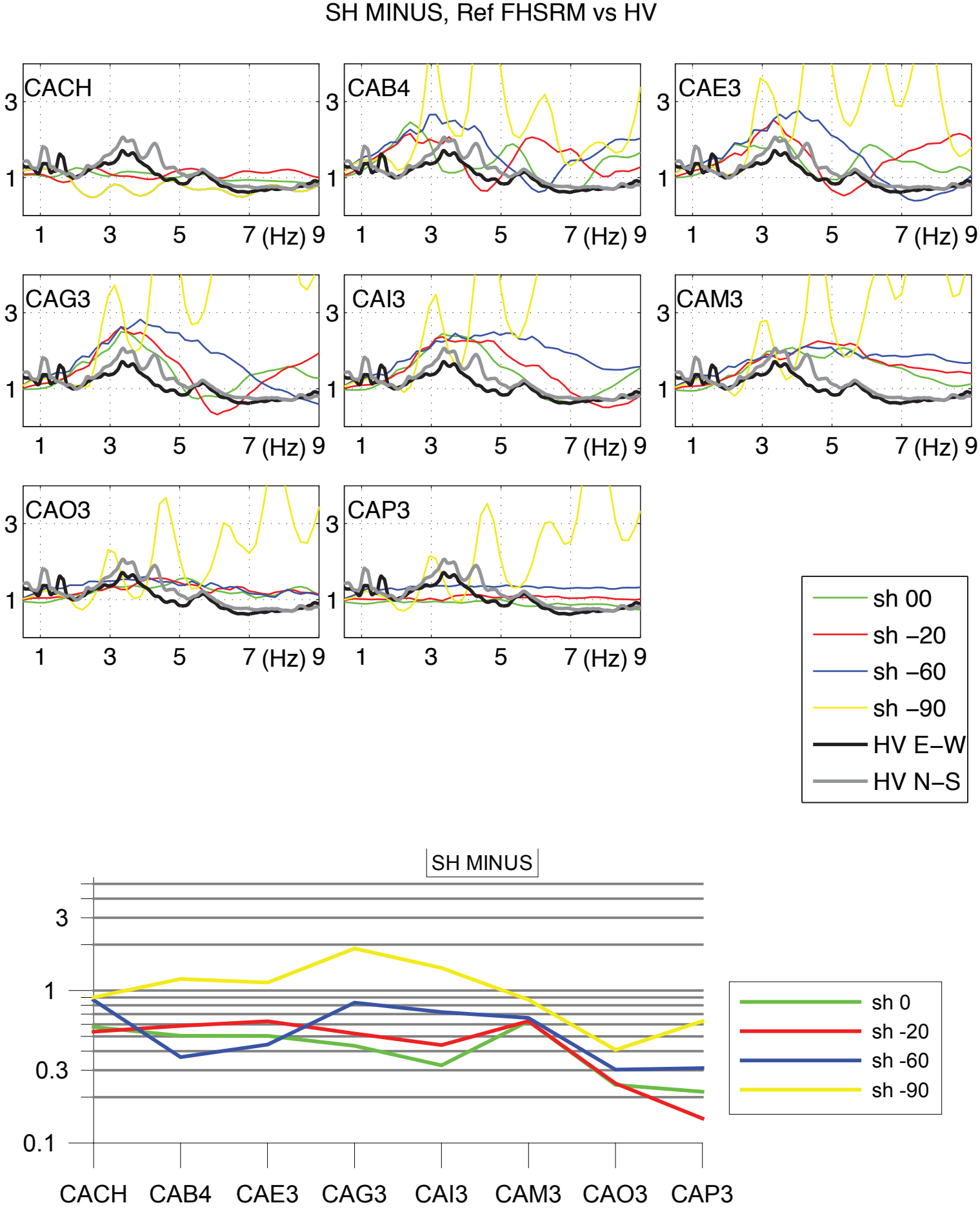
SH MINUS, Ref FHSRM vs HV
CACH
CAB4
CAE3
CAG3
CAI3
CAM3
CAO3
CAP3
3
1
1 3 5 7 (Hz) 9
sh 00
sh –20
sh –60
sh –90
HV E–W
HV N–S
SH MINUS
3
1
0.3
0.1
CACH CAB4 CAE3 CAG3 CAI3 CAM3 CAO3 CAP3
sh 0
sh -20
sh -60
sh -90

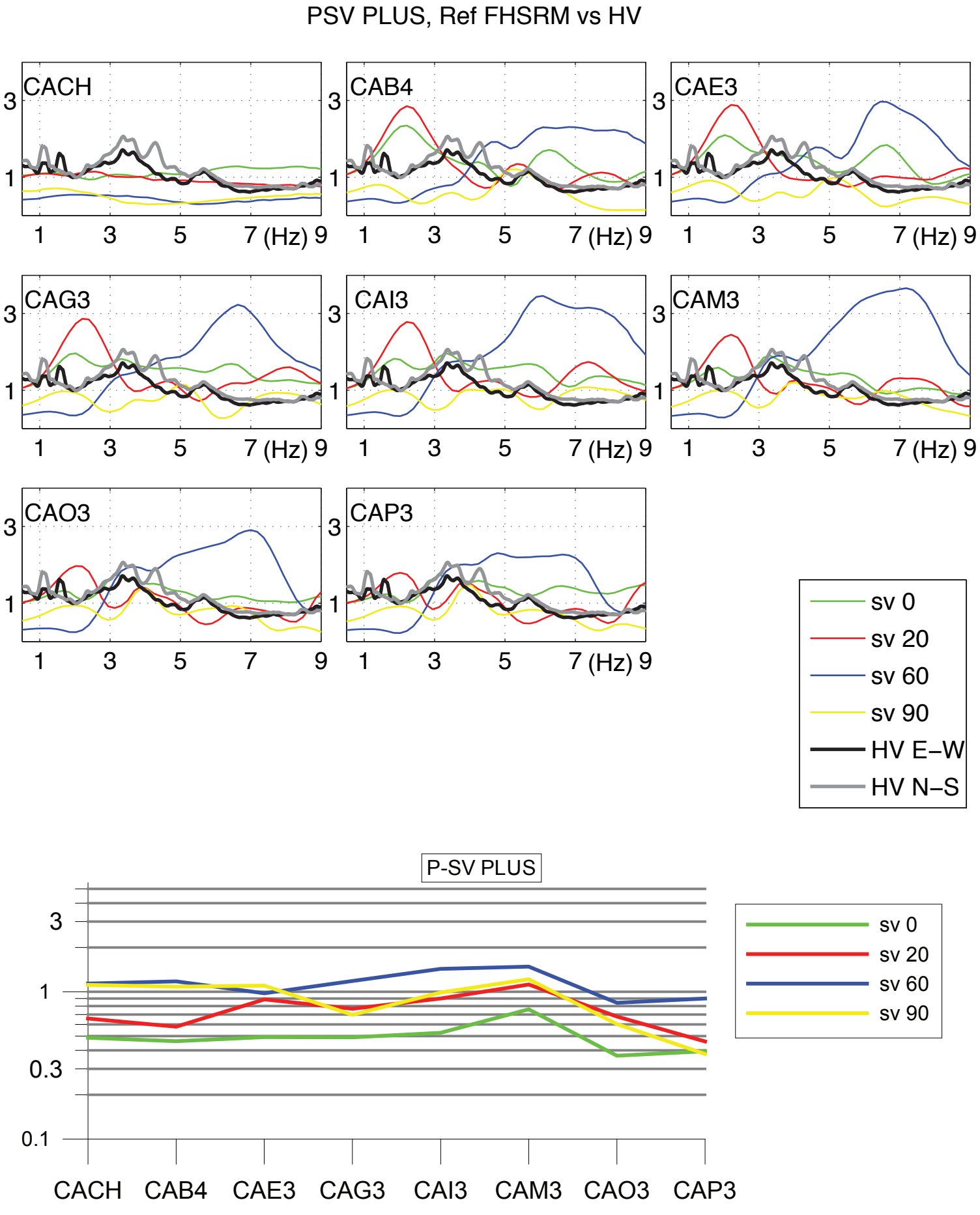
PSV PLUS, Ref FHSRM vs HV
CACH
CAB4
CAE3
CAG3
CAI3
CAM3
CAO3
CAP3
3
1
1 3 5 7 (Hz) 9
sv 0
sv 20
sv 60
sv 90
HV E–W
HV N–S

P-SV PLUS
3
1
0.3
0.1
CACH CAB4 CAE3 CAG3 CAI3 CAM3 CAO3 CAP3
sv 0
sv 20
sv 60
sv 90

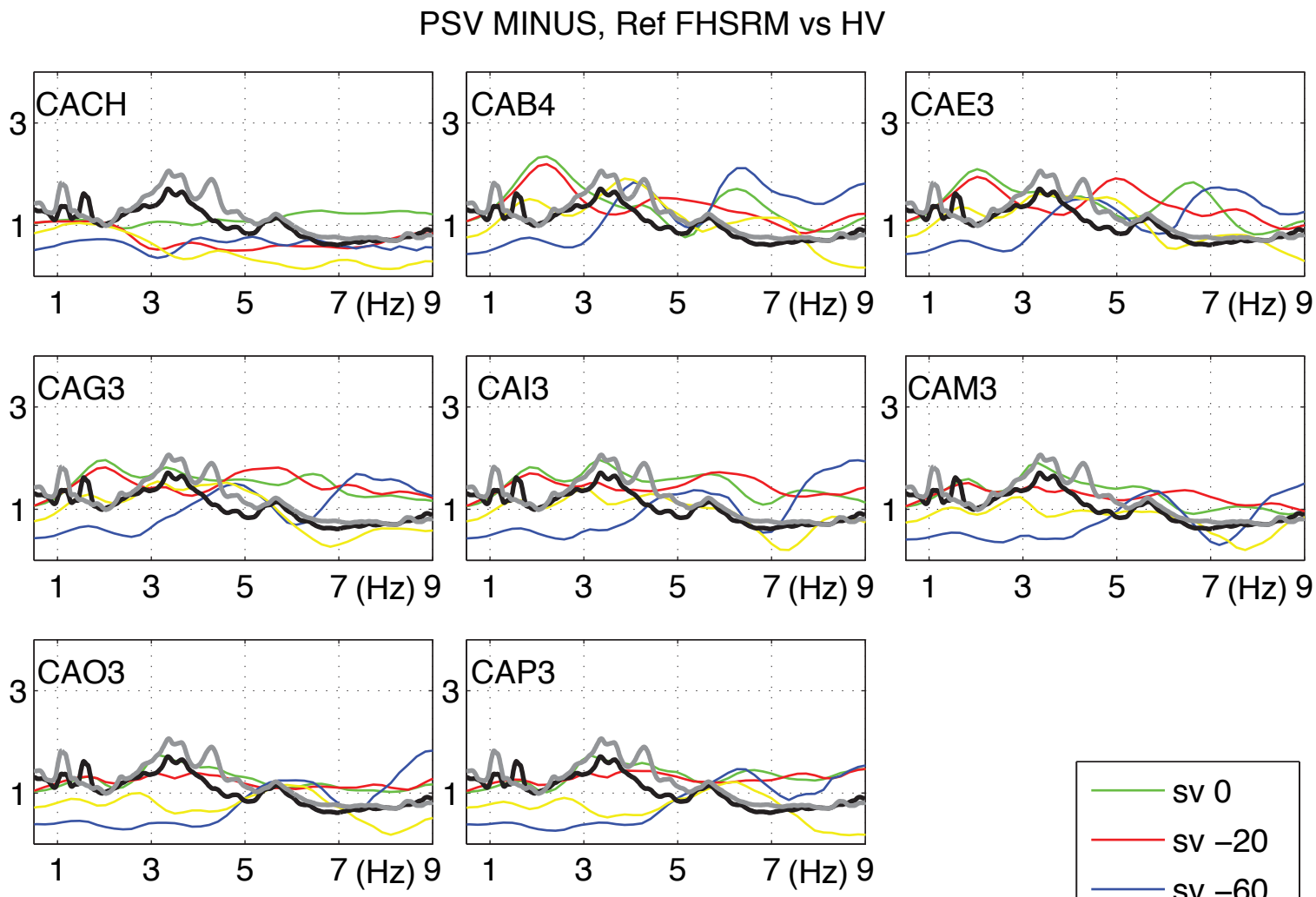
PSV MINUS, Ref FHSRM vs HV
CACH
CAB4
CAE3
CAG3
CAI3
CAM3
CAO3
CAP3
3
1
1 3 5 7 (Hz) 9
sv 0
sv –20
sv –60
sv –90
HV E–W
HV N–S

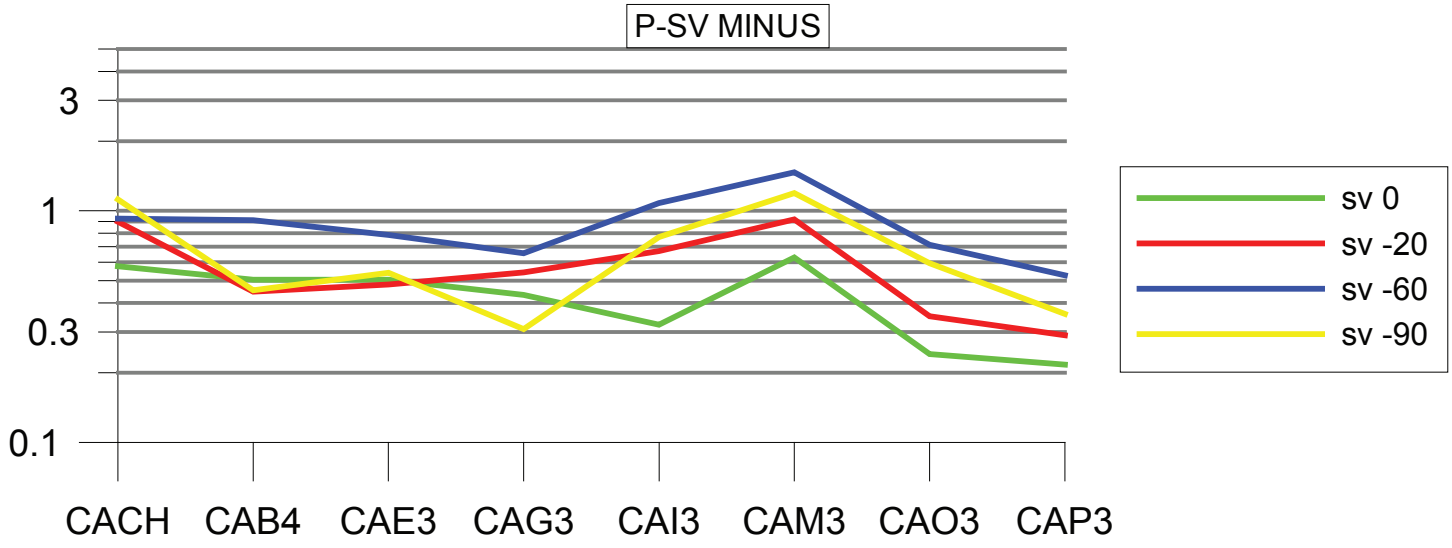
P-SV MINUS
3
1
0.3
0.1
CACH
CAB4
CAE3
CAG3
CAI3
CAM3
CAO3
CAP3
sv 0
sv -20
sv -60
sv -90

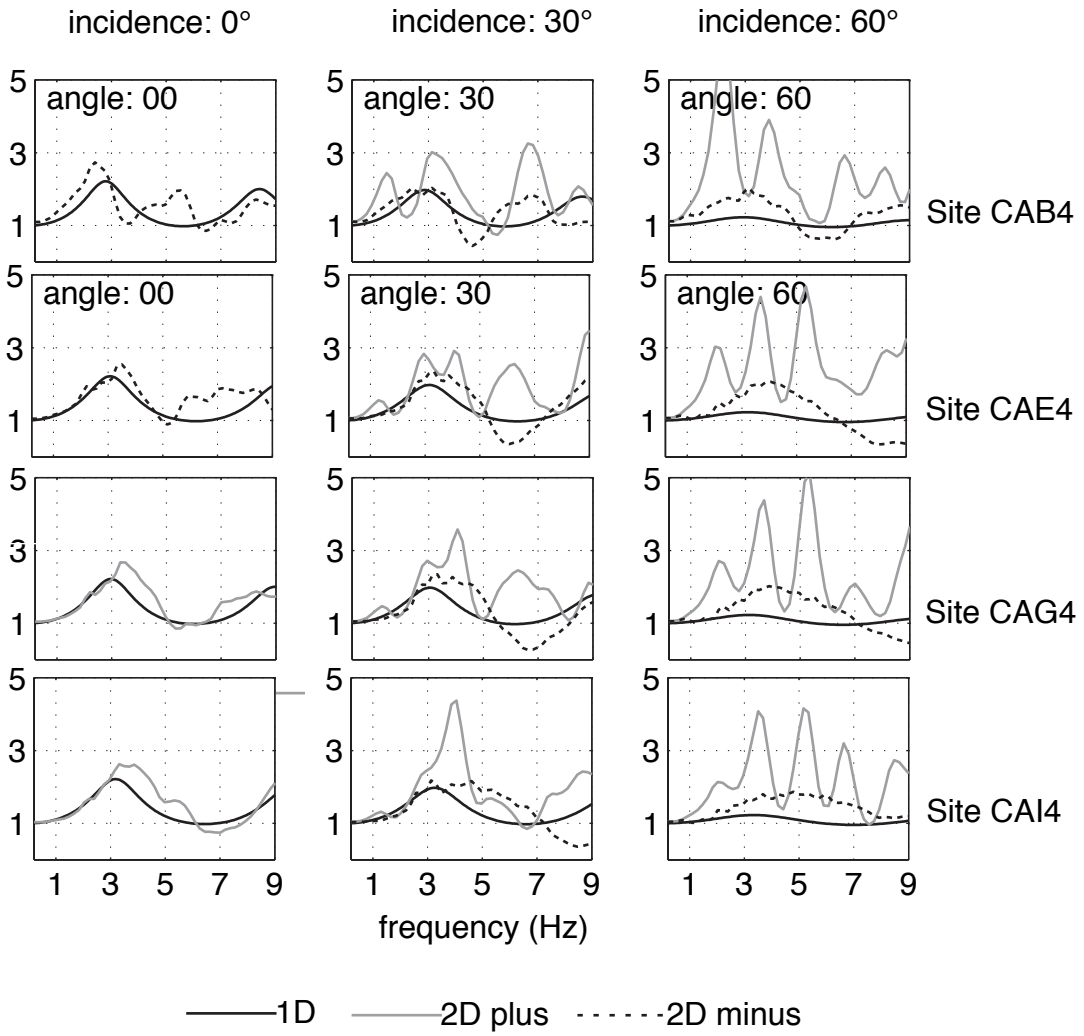
SH waves
incidence: 0°
incidence: 30°
incidence: 60°
angle: 00
angle: 30
angle: 60
Site CAB4
Site CAE4
Site CAG4
Site CAI4
5
3
1
1 3 5 7 9
frequency (Hz)
1D
2D plus
2D minus

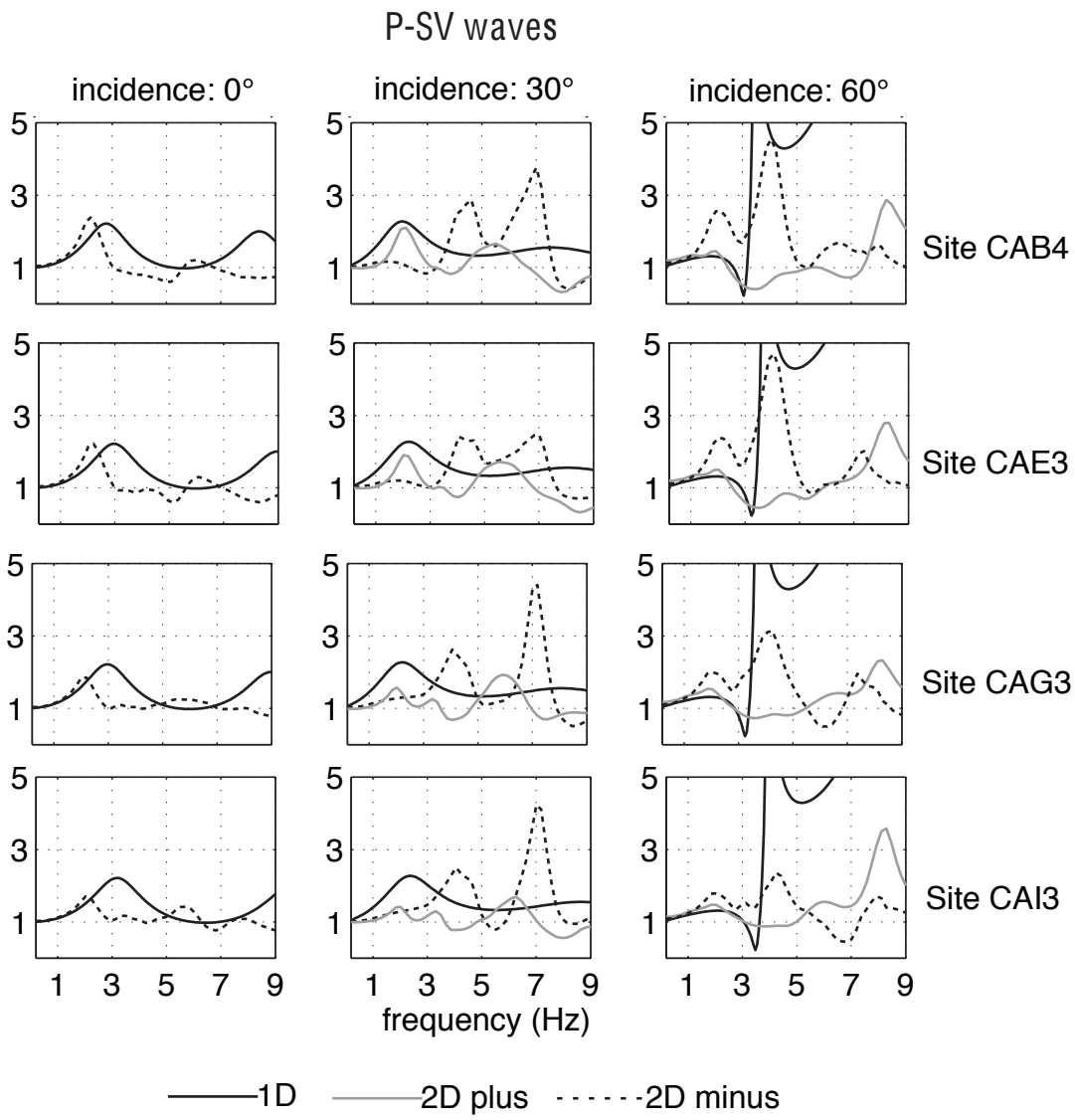
P-SV waves
incidence: 0°
incidence: 30°
incidence: 60°
Site CAB4
Site CAE3
Site CAG3
Site CAI3
5
3
1
1 3 5 7 9
frequency (Hz)
1D
2D plus
2D minus